

# Top-down control of flight by a non-canonical cortico-amygda pathway

<https://doi.org/10.1038/s41586-023-06912-w>

Received: 20 January 2022

Accepted: 29 November 2023

Published online: 17 January 2024

 Check for updates

Chandrashekhar D. Borkar<sup>1,2</sup>, Claire E. Stelly<sup>1,2,3</sup>, Xin Fu<sup>2,4</sup>, Maria Dorofeikova<sup>1,2</sup>, Quan-Son Eric Le<sup>2,4</sup>, Rithvik Vutukuri<sup>2,4</sup>, Catherine Vo<sup>2,4</sup>, Alex Walker<sup>2,4</sup>, Samhita Basavanhalli<sup>2,4</sup>, Anh Duong<sup>2,4</sup>, Erin Bean<sup>2,4</sup>, Alexis Resendez<sup>1,2</sup>, Jones G. Parker<sup>5</sup>, Jeffrey G. Tasker<sup>2,6</sup> & Jonathan P. Fadok<sup>1,2,✉</sup>

Survival requires the selection of appropriate behaviour in response to threats, and dysregulated defensive reactions are associated with psychiatric illnesses such as post-traumatic stress and panic disorder<sup>1</sup>. Threat-induced behaviours, including freezing and flight, are controlled by neuronal circuits in the central amygdala (CeA)<sup>2</sup>; however, the source of neuronal excitation of the CeA that contributes to high-intensity defensive responses is unknown. Here we used a combination of neuroanatomical mapping, *in vivo* calcium imaging, functional manipulations and electrophysiology to characterize a previously unknown projection from the dorsal peduncular (DP) prefrontal cortex to the CeA. DP-to-CeA neurons are glutamatergic and specifically target the medial CeA, the main amygdalar output nucleus mediating conditioned responses to threat. Using a behavioural paradigm that elicits both conditioned freezing and flight, we found that CeA-projecting DP neurons are activated by high-intensity threats in a context-dependent manner. Functional manipulations revealed that the DP-to-CeA pathway is necessary and sufficient for both avoidance behaviour and flight. Furthermore, we found that DP neurons synapse onto neurons within the medial CeA that project to midbrain flight centres. These results elucidate a non-canonical top-down pathway regulating defensive responses.

In the face of threat, organisms exhibit a continuum of defensive behaviours and flexibly shift between defensive strategies<sup>3,4</sup>. Engaging in the appropriate action for survival requires consideration of the proximity and intensity of the threat and the context of the encounter<sup>5,6</sup>. Moreover, exaggerated responses to perceived threats have been associated with anxiety, post-traumatic stress disorder, panic disorders and phobias<sup>1,7–9</sup>. Abnormal patterns of activation in the prefrontal cortex (PFC) are associated with these disorders, and bidirectional projections between the medial PFC (mPFC) and basolateral amygdala are part of a canonical pathway that has been extensively studied in the acquisition and expression of learned fear measured with freezing<sup>10–14</sup>. Previous studies have shown that animals exhibit behavioural scaling to favour flight over freezing in response to a high-intensity threat, and conditional freeze-to-flight shifting is regulated by distinct and mutually inhibitory local circuit motifs in the CeA<sup>2,15,16</sup>. Whether the cortex exerts top-down control of these behavioural shifts is not known. Interestingly, the mPFC also projects to the CeA<sup>17</sup>, raising the possibility that a direct pathway from mPFC to CeA could influence defensive action selection. However, this pathway has never been defined neuroanatomically, and its role in regulating defensive behaviour is unknown.

## Direct mPFC projections to medial CeA

To determine which subdivision of the mPFC projects to the CeA, we injected fluorescent, retrogradely trafficked latex microspheres into

the CeA (Fig. 1a,b). We observed sparse projections from both the pre-limbic and infralimbic cortices. However, a significantly greater number of CeA projectors were located in the DP nucleus (Fig. 1c,d and Extended Data Fig. 1a), a region of the mPFC recently linked to physiological and behavioural responses to stress<sup>18</sup>.

The mPFC regulates cognition, motivation and emotion through distinct glutamatergic projections to cortical and subcortical regions<sup>19</sup>. Vesicular glutamate transporter 1 (VGLUT1; also known as SLC17A7) labels most excitatory cortical neurons, yet the DP is enriched in both the VGLUT1 and VGLUT2 (also known as SLC17A6) isoforms, which define different populations of projection neurons<sup>20</sup>. To characterize the DP-to-CeA pathway more precisely, we injected a Cre-dependent mCherry vector into the DP of VGLUT1- or VGLUT2-Cre mice and quantified the fibre density in CeA subnuclei (Fig. 1e–g). We found that, although the mCherry<sup>+</sup> fibre density within the CeA was significantly higher in VGLUT1 mice (Fig. 1h–j), notably, in both VGLUT1 and VGLUT2 mice, mCherry<sup>+</sup> fibres were most abundant in the medial subdivision of the CeA (CeM), as compared to the lateral (CeL) or capsular subdivision (Fig. 1j). Therefore, VGLUT1- and VGLUT2-expressing DP neurons are anatomically positioned to influence the function of the primary amygdalar output centre controlling the expression of adaptive behaviour.

The DP also projects to the dorsomedial hypothalamus (DMH), a pathway known to regulate sympathetic responses to psychosocial stress<sup>18</sup>. To determine whether the DP-to-CeA and DP-to-DMH pathways are discrete, we injected red- or green-fluorescent retro-beads into

<sup>1</sup>Department of Psychology, Tulane University, New Orleans, LA, USA. <sup>2</sup>Tulane Brain Institute, Tulane University, New Orleans, LA, USA. <sup>3</sup>Department of Psychological Sciences, Loyola University, New Orleans, LA, USA. <sup>4</sup>Neuroscience Program, Tulane University, New Orleans, LA, USA. <sup>5</sup>Department of Neuroscience, Feinberg School of Medicine, Northwestern University, Chicago, IL, USA. <sup>6</sup>Department of Cell and Molecular Biology, Tulane University, New Orleans, LA, USA. <sup>✉</sup>e-mail: jfadok@tulane.edu

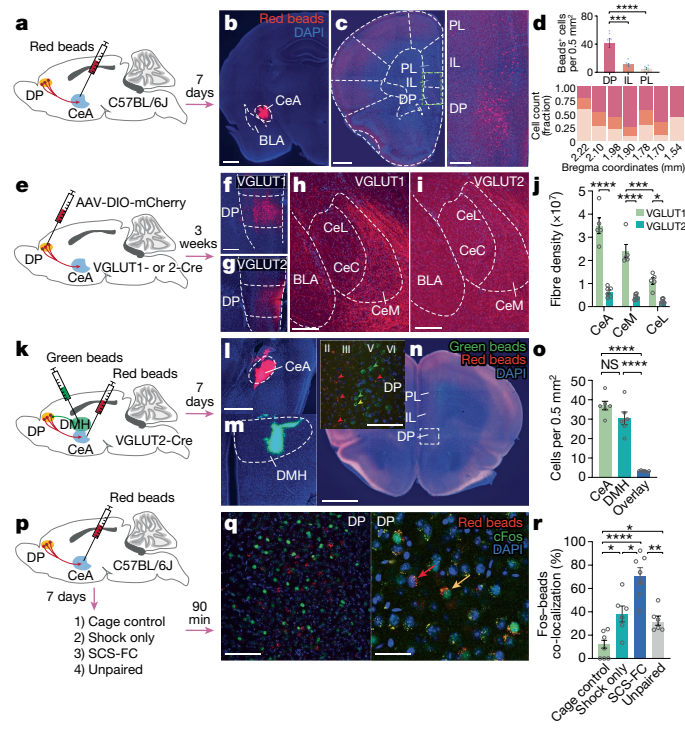


**Fig. 1 | Neuroanatomical characterization of the DP-to-CeA pathway.**

**a**, Retrograde tracing strategy. **b**, Representative targeting of red beads in the CeA. DAPI, 4',6-diamidino-2-phenylindole; BLA, basolateral amygdala. Scale bar, 500 µm. **c**, Representative bead localization in the mPFC. PL, prelimbic cortex; IL, infralimbic cortex. Scale bars, 500 µm (left) and 200 µm (right). **d**, Top: significantly more CeA-projecting neurons are localized in the DP, compared to that in the infralimbic or prelimbic cortex (one-way analysis of variance (ANOVA),  $F_{2,15} = 21.86, P < 0.0001$ ; Bonferroni's post hoc test;  $n = 6$  mice). Bottom: distribution of CeA-projecting neurons along the mPFC antero-posterior axis ( $n = 6$  mice; 4–6 sections per mouse). **e**, Anterograde tracing strategy. **f**, Representative image of DP targeting in VGLUT1-Cre mice. Scale bar, 200 µm. **g**, Representative image of DP targeting in VGLUT2-Cre mice. **h**, Representative expression of mCherry<sup>+</sup> terminals in the CeA of a VGLUT1-Cre mouse. CeC, capsular subdivision of the CeA. Scale bar, 200 µm. **i**, Representative expression of mCherry<sup>+</sup> terminals in the CeA of a VGLUT2-Cre mouse. Scale bar, 200 µm. **j**, Density of mCherry<sup>+</sup> fibres from VGLUT1<sup>+</sup> ( $n = 5$  mice, 3–4 sections per mouse) and VGLUT2<sup>+</sup> ( $n = 6$  mice, 2–3 sections per mouse) neurons (unpaired *t*-test for total CeA,  $t = 8.89, df = 9, P < 0.0001$ ; two-way ANOVA, CeM versus CeL, strain by region,  $F_{2,27} = 14.90, P < 0.0001$ ; Bonferroni's post hoc test). CeL includes lateral and capsular subregions. **k**, Dual-target retrograde tracing strategy from CeA and DMH. **l**, Representative targeting of DMH. **m**, Deposition of green and red beads in the mPFC. Inset: distribution of CeA and DMH projectors in different layers of DP. Red, green and yellow arrowheads indicate red beads, green beads and overlay, respectively. Scale bars, 500 µm (main image) and 100 µm (inset). **o**, Number of DP neurons projecting to CeA, DMH or both (one-way ANOVA,  $F_{2,15} = 62.06, P = 0.0001$ ; Bonferroni's post hoc test;  $n = 6$  mice, 3 sections per mouse). **p**, Strategy for neuronal activation analysis. **q**, Representative images showing bead-positive and/or Fos<sup>+</sup> cells in the DP. Red arrow, bead-positive; yellow arrow, bead-positive and Fos<sup>+</sup>. Scale bars, 100 µm (left) and 50 µm (right). **r**, Fos expression in bead-positive cells ( $n = 6$  mice for shock only and unpaired,  $n = 7$  mice for cage control and SCS-FC groups; 3–4 sections per mouse; one-way ANOVA,  $F_{3,22} = 22.01, P < 0.0001$ ; Bonferroni's post hoc test). Data in **d,j,o,r** are presented as means  $\pm$  s.e.m. Two-sided statistical tests were used. \*\*\* $P < 0.0001$ , \*\* $P < 0.001$ , \*\* $P < 0.01$ , \* $P < 0.05$ ; NS, not significant.

the CeA and DMH (Fig. 1k–m). Both red and green retro-beads were localized in DP cells (Fig. 1n), but the DMH-projecting DP neurons were localized in layers V and VI (90% versus 8.7% in layers II and III), whereas

CeA-projecting cells were found mostly in layers II and III (Fig. 1n, inset, and Extended Data Fig. 1b; 87% versus 10.5% in layers V and VI). Only a small number of DP cells (about 7%) were co-labelled, suggesting that the DP-to-CeA and DP-to-DMH pathways are anatomically distinct (Fig. 1o and Extended Data Fig. 1b).

Given the role of the CeA in defensive response selection and the role of the DP in stress responding<sup>2,18</sup>, we reasoned that threats would activate CeA-projecting DP neurons. To test this, we injected C57BL/6J mice with retro-beads in the CeA and divided animals into four groups: home cage control, footshock only, unpaired and fear conditioning (FC; Fig. 1p). The FC group was subjected to a protocol that we developed that elicits freezing and flight responses to separate components of a serial compound stimulus<sup>2</sup> (SCS-FC; Extended Data Fig. 1d,e). Compared to home cage control, shock only and unpaired groups, SCS-FC mice exhibited significantly greater numbers of retro-bead<sup>+</sup> cells co-labelled with Fos (Fig. 1q,r). There were no significant differences in the total number of retro-bead<sup>+</sup> cells across the groups, indicating a consistent retrograde labelling efficiency across the experimental groups (Extended Data Fig. 1c).

## DP-to-CeA neurons are activated by flight

The significantly elevated expression level of Fos in the SCS-FC group suggests that DP-to-CeA neurons are recruited most under conditions that elicit robust cue-induced defensive behaviour. Therefore, we set out to determine the activation patterns of DP-to-CeA projection neurons during the SCS-FC protocol, which induces escalating intensities of defensive behaviours in a context-specific manner (Extended Data Fig. 1d,e). We used an intersectional approach to selectively express GCaMP6f in DP-to-CeA projection neurons and imaged *in vivo* calcium activity in freely moving mice using custom-built open-source minisscopes (Fig. 2a–c). We observed low levels of freezing and no flight before conditioning (Extended Data Fig. 2a–d), with similar levels of neuronal activation to the tone and white noise (WN) components of the SCS (Extended Data Fig. 2e–j;  $n = 221$  neurons from 6 mice). Moreover, there was no correlation between calcium activity and movement speed before conditioning (Extended Data Fig. 2g). Following conditioning, mice exhibited elevated levels of freezing in response to the tone, and elevated levels of flight in response to the WN, in the conditioning context in which footshocks occur (hereafter called the high-threat context; Fig. 2d,e and Extended Data Fig. 3a,b;  $n = 273$  neurons from 6 mice)<sup>2,21</sup>. By contrast, mice exhibited predominantly freezing when exposed to the same conditioned stimuli in a neutral context in which shocks never occur (hereafter called the low-threat context; Fig. 2m,n and Extended Data Fig. 3i,j;  $n = 176$  neurons from 6 mice). Notably, as conditioning progressed, the mean activity of CeA-projecting DP neurons increased concurrently, which correlated significantly with speed in the high- but not low-threat context (Extended Data Fig. 3c,k).

In the high-threat context, the CeA-projecting DP neuronal population was most active during WN and shock (Fig. 2f–i), with many individual DP-to-CeA neurons active specifically during sensory epochs eliciting flight behaviour (WN and post-shock periods, 45% of recorded neurons; Fig. 2g,h and Extended Data Fig. 3g,h). Only 2% of cells encoded the tone (Fig. 2h) and average neuronal activity was significantly higher during WN and post-shock compared to that during the tone (Fig. 2i). Notably, WN-induced activation was diminished in the low-threat context (Fig. 2o), neuronal responses were more evenly distributed across sensory epochs (Fig. 2p,q), and no significant difference was observed between neuronal responses to tone and WN (Fig. 2r and Extended Data Fig. 3o,p). Together, these data suggest that DP-to-CeA neuronal activity is context-dependent and is more associated with sensory stimuli that induce higher-intensity threat behaviour.

To determine whether DP-to-CeA projector activity is associated with defensive responses, we analysed neuronal activity around the

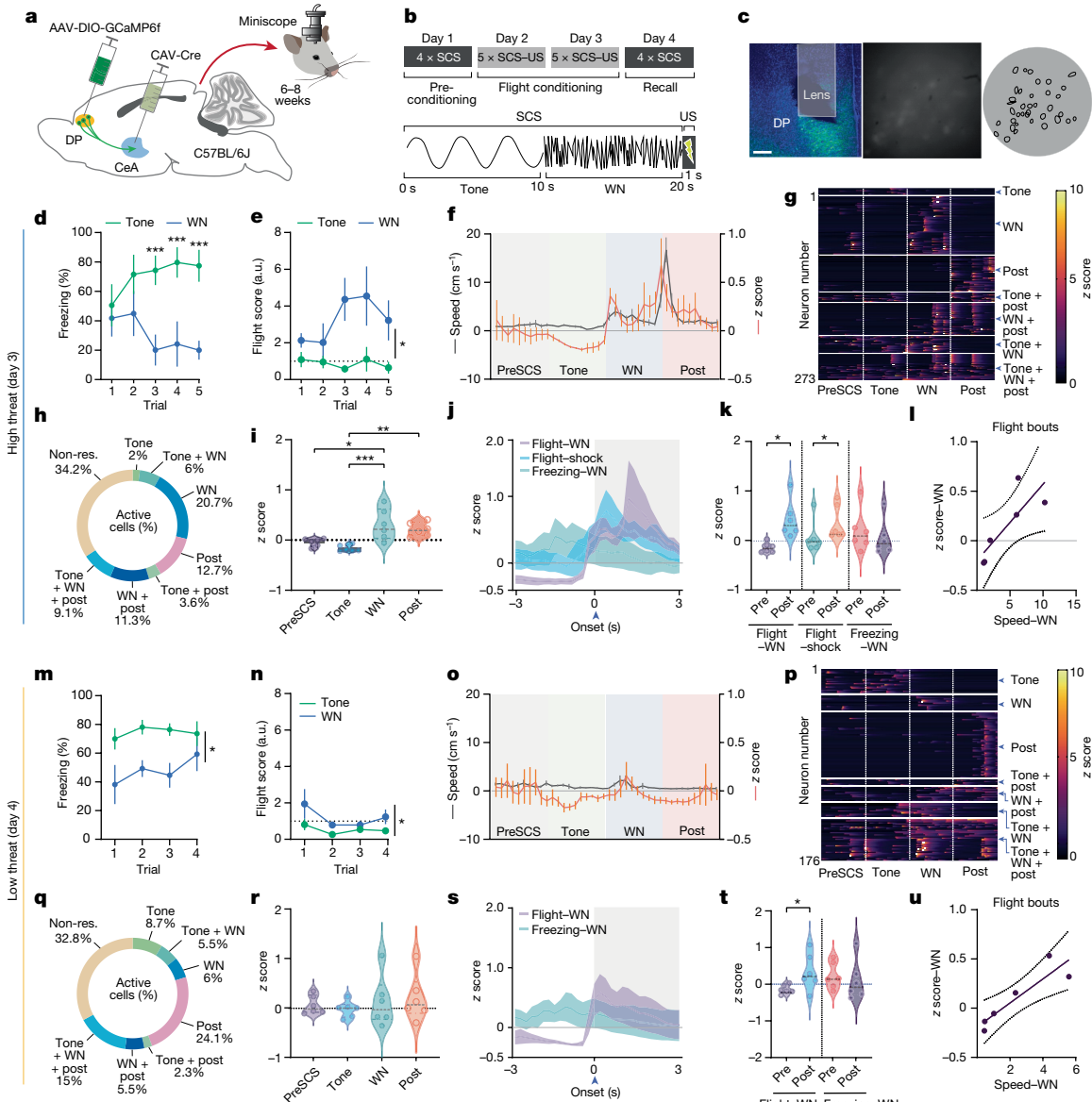


**Fig. 2 | DP-to-CeA projection cells are activated by high-fear states.**

**a**, Intersectional strategy used to record DP-to-CeA projector activity ( $n = 6$  mice for all panels). The image of the mouse head was reproduced from SciDraw. **b**, Mice were subjected to a paradigm designed to elicit conditioned freezing and flight. US, unconditioned stimulus **c**, Left: representative GCaMP6f expression and lens placement. Scale bar, 500  $\mu$ m. Right: miniscope field of view (raw and post cell extraction). **d**, Freezing in response to cues in the high-threat context ( $n = 6$  mice; two-way ANOVA, trial by stimuli,  $F_{4,20} = 4.354$ ,  $P = 0.01$ , followed by Bonferroni's post hoc test). **e**, Cue-induced flight in the high-threat context ( $n = 6$  mice; two-way ANOVA, trial by stimuli,  $F_{4,20} = 2.08$ ,  $P = 0.12$ , stimuli,  $F_{1,5} = 13.49$ ,  $P = 0.014$ , trial,  $F_{4,20} = 0.933$ ,  $P = 0.46$ ). a.u., arbitrary units. **f**, Population activity and speed from the last trial in the high-threat context ( $n = 273$  cells). **g**, Neuronal activity of individual neurons during the last trial in the high-threat context ( $n = 273$  cells). **h**, Percentages of neurons activated during different cue periods in the high-threat context. Non-res., non-responsive neurons. **i**, Average neuronal activity from all trials in the high-threat context ( $n = 273$  cells; one-way ANOVA,  $F_{3,20} = 9.33$ ,  $P = 0.005$ ; Bonferroni's post hoc test). **j**, Neuronal activity aligned at onset of freezing and flight in the high-threat context ( $n = 273$  cells). **k**, Population activity 3 s before and after the onset of freezing and flight ( $n = 273$  cells; paired  $t$ -test flight-WN,  $t = 3.28$ ,  $df = 5$ ; Mann-Whitney test, flight-shock; paired  $t$ -test freezing-WN,  $t = 1.778$ ,  $df = 5$ ,  $P = 0.13$ ). **l**, Spearman correlation of neuronal activity and speed

aligned to WN-induced flight bouts ( $n = 273$  cells;  $r = 0.94$ , 95% confidence interval (CI) = 0.003864–0.1503, each point = 1 s). **m**, Freezing in response to cues in the low-threat context ( $n = 6$  mice; two-way ANOVA, trial by stimuli,  $F_{3,15} = 0.5806$ ,  $P = 0.63$ , stimuli,  $F_{1,5} = 11.73$ ,  $P = 0.018$ , trial,  $F_{3,15} = 0.83$ ,  $P = 0.490$ ). **n**, Cue-induced flight in the low-threat context ( $n = 6$  mice; two-way ANOVA, trial by stimuli,  $F_{3,15} = 1.58$ ,  $P = 0.23$ , stimuli,  $F_{1,5} = 8.12$ ,  $P = 0.035$ , trial,  $F_{3,15} = 1.42$ ,  $P = 0.27$ ). **o**, Population activity and speed from the last trial in the low-threat context ( $n = 176$  cells). **p**, Neuronal activity of individual neurons during the last trial in the low-threat context ( $n = 176$  cells). **q**, Percentages of neurons activated during different cue periods in the low-threat context. **r**, Average neuronal activity from all trials in the low-threat context ( $n = 176$  cells; one-way ANOVA, effect of stimuli  $F_{3,20} = 0.39$ ,  $P = 0.75$ ). **s**, Neuronal activity aligned to the onset of WN-induced freezing and flight in the low-threat context ( $n = 176$  cells). **t**, Population activity 3 s before and after the onset of freezing and flight ( $n = 176$  cells; paired  $t$ -test flight-WN,  $t = 2.58$ ,  $df = 5$ ; flight-post,  $t = 0.8493$ ,  $df = 5$ ,  $P = 0.43$ ; freezing-WN,  $t = 0.8493$ ,  $df = 5$ ,  $P = 0.43$ ). **u**, Spearman correlation of neuronal activity and speed aligned to WN-induced flight bouts ( $n = 176$  cells;  $r = 0.94$ , 95% CI = 0.04251–0.2010; each point = 1 s). Data in **d–f, j, m–o, s** are presented as means  $\pm$  s.e.m. Violin plots in **i, k, l, r, t** indicate median, interquartile range and the distribution of individual data points. Two-sided statistical tests were used. \*\*\* $P < 0.001$ , \*\* $P < 0.01$ , \* $P < 0.05$ .

onset of freezing and flight bouts in both contexts. In the high-threat context, neuronal activity was significantly increased at the onset of flight yet was unchanged in response to freezing (Fig. 2j,k). Neuronal activity was also positively correlated with speed during flight bouts (Fig. 2l and Extended Data Fig. 3d), but not with locomotion surrounding freezing bouts (Extended Data Fig. 3e,f). Flight occasionally occurs in the low-threat context; therefore, we also analysed neuronal responses to flight and freezing onset under these conditions. Just as in the high-threat context, there was a significant increase in activity following flight onset, and a significant correlation between neuronal activation and speed during flight, yet no increase in activity was noted for freezing (Fig. 2s–u and Extended Data Fig. 3l–n).

## DP-to-CeA neurons mediate avoidance

The prevalence of DP-to-CeA neurons active in the high-threat context suggests a functional role for this pathway in negative-valence-related behaviours. We first tested this idea using chemogenetic manipulations of DP-to-CeA neurons in standard avoidance paradigms used to assay anxiety-like states: the open field test (OFT) and the elevated plus maze (EPM). We used an intersectional targeting strategy to express either inhibitory (hM4Di-mCherry) or excitatory (hM3Dq-mCherry) designer receptors exclusively activated by designer drugs (DREADDs) in the DP-to-CeA pathway, with an mCherry group serving as a clozapine *N*-oxide (CNO) control (Fig. 3a–c). DREADD-mediated inhibition of the DP-to-CeA pathway increased the time spent and number of entries in the centre zone of the OFT (Fig. 3d,f,g), as well as increasing the number of entries into the open arm of the EPM (Fig. 3e,i,j) without affecting the total distance travelled (Fig. 3h). By contrast, chemogenetic stimulation of this pathway did not induce avoidance behaviour in either assay. These findings suggest that the DP-to-CeA pathway is necessary but not sufficient for innate avoidance behaviour.

## DP-to-CeA neurons mediate flight

To study the necessity of the DP-to-CeA pathway in other forms of defensive behaviour, we carried out optogenetic loss-of-function studies in the OFT and SCS-FC (Fig. 4a–f and Extended Data Fig. 4). We injected a Cre-dependent vector carrying eNpHR or eYFP control into the DP, and a retrograde CAV2-Cre vector into the CeA of C57BL/6J mice (Fig. 4a and Extended Data Fig. 4a). Inhibition of DP-to-CeA terminals significantly increased the time spent in, and number of entries into, the centre zone of the OFT, but did not affect locomotor activity, consistent with chemogenetic inhibition (Extended Data Fig. 4c–e). We then used a within-subjects experimental design in the SCS-FC paradigm, with optogenetic stimulation during half of the trials (Extended Data Fig. 4b). In the high-threat context, inhibition of DP-to-CeA terminals significantly reduced the level of WN-induced flight (Fig. 4e and Extended Data Fig. 4g,h). Notably, inhibiting these terminals reduced the level of freezing in response to the tone in the eNpHR group, yet also elevated the level of freezing during the WN period, demonstrating cue-specific reduction in defensive response intensity but not a complete inhibition of fear<sup>22,23</sup> (Fig. 4d and Extended Data Fig. 4f). Optogenetic inhibition had no effect on defensive behaviour in the low-threat context (Fig. 4f and Extended Data Fig. 4i–k), further supporting the context-dependent function of the DP-to-CeA pathway.

To study the sufficiency of the DP-to-CeA pathway in mediating flight, anxiety and aversive behaviour, we carried out optogenetic gain-of-function studies (Fig. 4g–r and Extended Data Figs. 5–8). Optogenetic activation of DP-to-CeA terminals using a non-cell-type-specific intersectional approach (Extended Data Fig. 5a) did not elicit significant changes in negative-valence behaviours (Extended Data Fig. 5b–j). Stimulation of DP terminals in the CeA expressing ChR2 under the

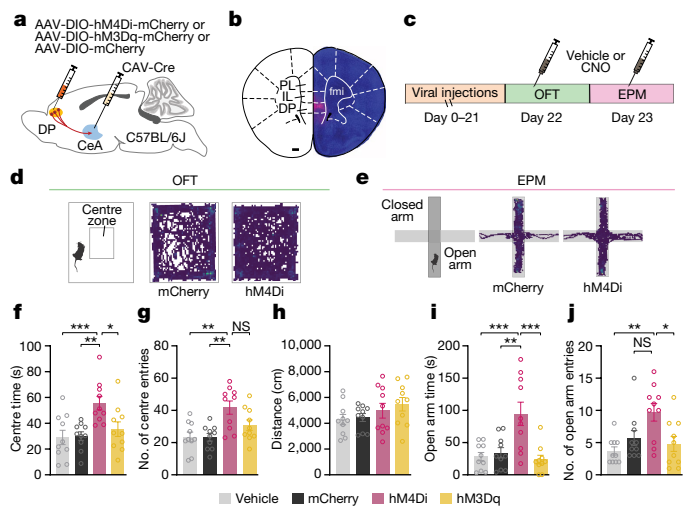


**Fig. 3 | Chemogenetic inhibition of the DP-to-CeA pathway reduces avoidance.** **a**, Intersectional strategy used for chemogenetic manipulation of the DP-to-CeA pathway. **b**, Representative mCherry expression in the DP, fmi, forceps minor of the corpus callosum. Scale bar, 500 µm. **c**, Mice from control (DREADD + vehicle,  $n = 10$ ; mCherry + CNO,  $n = 10$  for f–j) and DREADD (hM4Di-mCherry,  $n = 10$ ; hM3Dq-mCherry,  $n = 10$  for f–j) groups were subjected to the OFT and EPM 30 min after CNO ( $5 \text{ mg kg}^{-1}$ ) or vehicle injection. **d**, Representative OFT activity plots of mCherry + CNO and hM4Di + CNO mice. **e**, Representative EPM activity plots of mCherry + CNO and hM4Di + CNO mice. **f**, Inhibition of the DP-to-CeA pathway significantly increased time spent in the centre zone (one-way ANOVA,  $F_{3,36} = 6.06, P = 0.001$ ; Bonferroni's post hoc test). **g**, Inhibition of the DP-to-CeA pathway significantly increased the number of entries in the centre zone (one-way ANOVA,  $F_{3,36} = 7.158, P = 0.0007$ ; Bonferroni's post hoc test). NS, not significant. **h**, DREADD manipulations did not alter distance travelled in the OFT (one-way ANOVA,  $F_{3,36} = 1.36, P = 0.270$ ). **i**, Inhibition of the DP-to-CeA pathway significantly increased open arm time in the EPM (one-way ANOVA,  $F_{3,36} = 9.22, P = 0.0001$ ; Bonferroni's post hoc test). **j**, Inhibition of the DP-to-CeA pathway significantly increased open arm entries in the EPM (one-way ANOVA,  $F_{3,36} = 5.47, P = 0.003$ ; Bonferroni's post hoc test). Data in f–j are presented as mean  $\pm$  s.e.m. Two-sided statistical tests were used. \*\*\* $P < 0.001$ , \*\* $P < 0.01$ , \* $P < 0.05$ .

control of a CaMKIIα promoter (Extended Data Fig. 6a) elicited a significant avoidance response (Extended Data Fig. 6b,c); however, there was no significant effect on freezing and flight responses in either threat context (Extended Data Fig. 6d–g).

The lack of effect of these manipulations on defensive behaviour could be due to functional heterogeneity in the DP-to-CeA pathway (Fig. 1j). Therefore, we separately targeted the VGLUT1<sup>+</sup> and VGLUT2<sup>+</sup> subpopulations and stimulated axon terminals in the CeA (Fig. 4g and Extended Data Figs. 7 and 8). Stimulation of VGLUT1<sup>+</sup> terminals induced real-time place preference (Extended Data Fig. 7b,c), and a reduction in cue-induced freezing (Extended Data Fig. 7d,f), but it had no effect on conditioned flight responses (Extended Data Fig. 7e,g). However, optogenetic activation of VGLUT2<sup>+</sup> terminals in the CeA (Extended Data Fig. 8a,b) induced significant place avoidance (Extended Data Fig. 8c) and a significant decrease in the number of centre entries in the OFT (Extended Data Fig. 8d,e). Stimulation of VGLUT2<sup>+</sup> terminals also significantly reduced the level of freezing (Fig. 4i,l and Extended Data Fig. 8f,i) and significantly elevated the level of flight in both contexts (Fig. 4j,k,m and Extended Data Fig. 8g,h,j).

We next tested the effects of VGLUT2<sup>+</sup> terminal stimulation on flight responses in the high-threat context in the absence of footshock (Fig. 4n–r). Optogenetic stimulation during WN significantly reduced the level of freezing (Fig. 4n,o) and increased the level of flight (Fig. 4p–r). Together, these data demonstrate that the DP-to-CeA pathway is necessary and sufficient for conditioned flight responses.

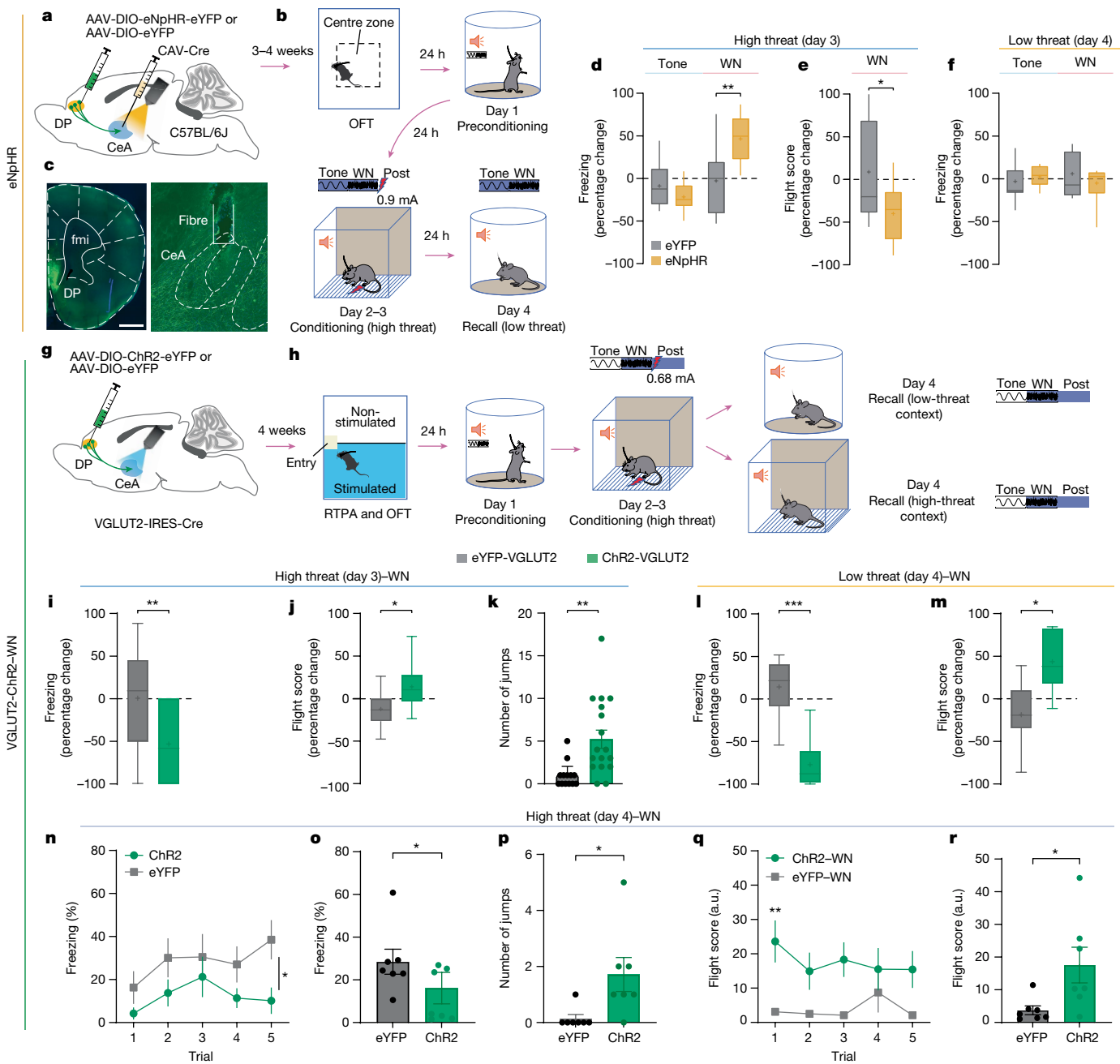


**Fig. 4 | Optogenetic modulation of the DP-to-CeA pathway regulates flight.**

**a**, Intersectoral targeting strategy for optogenetic inhibition of the DP-to-CeA pathway. **b**, Experimental timeline for optogenetic inhibition experiments. **c**, Representative images of eNpHR-eYFP expression in DP and fibre stub placement in CeA. Scale bar, 500  $\mu$ m. **d,e**, Effect of optogenetic inhibition in eYFP control ( $n = 9$ ) and eNpHR ( $n = 9$ ) groups on freezing (light-emitting diode (LED) on versus LED off) in the high-threat context (eYFP versus eNpHR, unpaired  $t$ -test; **d**) and flight scores (LED on versus LED off) in the high-threat context (eYFP versus eNpHR, unpaired  $t$ -test; **e**). **f**, Effect of optogenetic inhibition in eYFP control ( $n = 9$ ) and eNpHR ( $n = 9$ ) groups on freezing (LED on versus LED off) in the low-threat context (eYFP versus eNpHR, Mann–Whitney, not significant). **g**, Viral injection strategy for optogenetic stimulation of the DP-to-CeA pathway. **h**, Experimental timeline for optogenetic stimulation experiments. RTPA, real-time place aversion. **i–k**, Effect of optogenetic stimulation in eYFP control ( $n = 13$ ) or ChR2 ( $n = 17$ ) groups on freezing (LED on versus LED off; Mann–Whitney; **i**), flight scores (LED on versus LED off; unpaired  $t$ -test,  $t = 2.262$ ,  $df = 28$ ; **j**) and escape jumps (unpaired  $t$ -test,  $t = 3.383$ ,

$df = 28$ ; **k**) in the high-threat context. **l,m**, Effect of optogenetic stimulation in eYFP ( $n = 6$ ) and VGLUT2-ChR2 ( $n = 10$ ) groups on freezing (LED on versus LED off; unpaired  $t$ -test,  $t = 5.046$ ,  $df = 14$ ; **l**) and flight scores (LED on versus LED off; unpaired  $t$ -test,  $t = 2.845$ ,  $df = 14$ ; **m**) in the low-threat context. **n–r**, Effects of optogenetic stimulation in eYFP ( $n = 7$ ) and VGLUT2-ChR2 ( $n = 7$ ) groups during recall in the high-threat context on trial-wise freezing (two-way ANOVA, group by trial,  $F_{4,48} = 0.644$ ,  $P = 0.633$ , main effect of group,  $F_{1,12} = 4.874$ ,  $P = 0.0457$ ; **n**), average freezing (unpaired  $t$ -test,  $t = 2.208$ ,  $df = 12$ ; **o**), escape jumps (unpaired  $t$ -test,  $t = 2.524$ ,  $df = 12$ ; **p**), trial-wise flight scores (two-way ANOVA, trial by group,  $F_{4,48} = 2.738$ ,  $P = 0.0393$ ; Bonferroni's multiple comparisons test; **q**) and average flight scores (unpaired  $t$ -test,  $t = 2.462$ ,  $df = 12$ ; **r**). Box and whisker plots in **d–f,i,j,l,m** indicate median, interquartile range, and minimum to maximum of the distribution; crosses indicate means. Data in **k,n–r** are presented as mean  $\pm$  s.e.m. Two-sided statistical tests were used. \*\*\* $P < 0.001$ , \*\* $P < 0.01$ , \* $P < 0.05$ . The images of the mice in the recall context in **b,h** were reproduced from SciDraw.

## DP controls CeM outputs to the periaqueductal grey

To investigate how DP neurons might affect flight behaviour via the CeM, we first asked whether DP-to-CeA projections differentially innervate genetically defined cell types in the CeM that are known to mediate defensive behaviour in the CeL<sup>2</sup> (Extended Data Fig. 9a–i). There were many labelled terminals near both somatostatin (SOM)-positive and corticotrophin-releasing hormone (CRH)-positive somata in the CeM (Extended Data Fig. 9b), and DP fibre stimulation resulted in a strong induction of either a monophasic inward synaptic current or a biphasic inward–outward synaptic current in both SOM<sup>+</sup> and CRH<sup>+</sup> neurons in the CeM (Extended Data Fig. 9d,f,i), but not in the CeL (Extended Data Fig. 9e,h). These optogenetically evoked responses were blocked by bath application of the AMPA receptor antagonist DNQX (Extended Data Fig. 9g). These findings confirm the presence of functional glutamatergic DP projections to the CeM but also suggest that this pathway controls flight behaviour through a mechanism distinct from that which was previously described in the CeL.

CeM output neurons can be classified by their action potential firing properties<sup>24–26</sup>, with distinct subclasses influencing behavioural threat responding through their projections to known targets within the periaqueductal grey (PAG) region<sup>26–28</sup>. In particular, burst-firing and regular-firing neurons innervate the dorsolateral and lateral columns of the PAG (dIPAG and IPAG) involved in flight responses<sup>26,29,30</sup>. We tested whether DP innervation targeted physiologically defined CeM neuronal populations. We classified DP-excited CeM neurons as regular spiking, bursting or late firing (Fig. 5a–c and Extended Data Fig. 9j). Optogenetic stimulation of DP terminals in the CeA primarily evoked excitatory postsynaptic currents in burst-firing and regular-firing neurons, whereas late-firing neurons were only rarely excited (Fig. 5c), suggesting that the DP excites CeM projections to PAG columns linked to flight behaviour.

To directly test this hypothesis, we first labelled the neuroanatomical pathway by injecting an anterograde transneuronal AAV1-Cre vector into the DP region and a Cre-dependent mCherry-expressing vector into the CeM (Fig. 5d). This approach revealed numerous targets of CeM neurons receiving DP innervation (Extended Data Fig. 10). Quantifying the projection topography of the labelled CeM neurons in the PAG revealed that the IPAG, known to regulate flight<sup>28</sup>, had the highest density of mCherry<sup>+</sup> fibres (Fig. 5e–g). We then labelled CeM neurons projecting to different columns of the PAG and carried out whole-cell patch clamp recordings while optogenetically stimulating VGLUT2<sup>+</sup> DP afferents in CeM (Fig. 5h and Extended Data Fig. 10a–c). We observed that CeM projections to the dIPAG or IPAG have larger monosynaptic excitatory currents than projections to the ventrolateral PAG (vIPAG) in response to stimulation of DP terminals (Fig. 5i,j), despite there being no preferential innervation bias between the projection pathways (Fig. 5k). These data support the hypothesis that the DP promotes flight through excitation of CeM output neurons to columns of PAG known to be important for flight behaviour.

## Discussion

Here we define the function of a new top-down pathway from the DP region of the mPFC directly to the CeA in the control of defensive behaviour. This non-canonical corticolimbic pathway is distinct from the well-studied reciprocal pathway between the prelimbic and infralimbic cortices and the basolateral amygdala and is activated in high-threat situations. Glutamatergic DP neurons exert their influence on defensive behaviour through projections to the CeM, the amygdala output nucleus known for coordinating complex responses to threats. These findings have important implications for understanding the basic neurobiology of threat processing.

The DP contains populations of VGLUT1<sup>+</sup> and VGLUT2<sup>+</sup> glutamatergic neurons. We found that both populations innervate the CeM, and our optogenetic experiments revealed that excitation of VGLUT1<sup>+</sup>

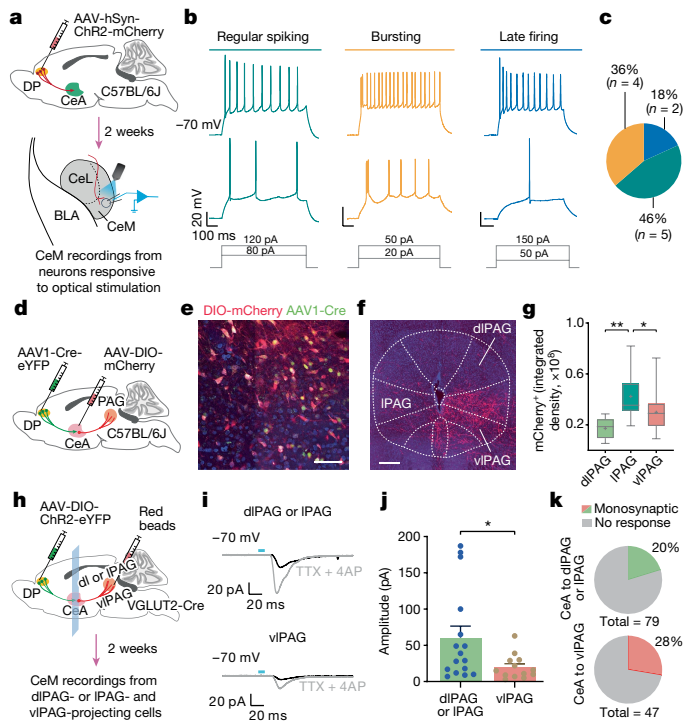


**Figure 5 | DP-to-CeA neurons exert excitatory control over CeM projections.** **a**, Injection targeting and recording strategy. **b**, Representative firing patterns evoked by depolarizing current injection in CeM neurons innervated by DP projections. DP innervation was confirmed by postsynaptic responses to optogenetic stimulation of ChR2<sup>+</sup> axons in CeM (data not shown). **c**, Proportion of DP-excited CeM neurons classified by firing patterns ( $n = 11$  cells from 4 mice). **d**, Viral targeting strategy used to map the PAG-projecting CeM neurons innervated by DP. **e**, Representative image showing expression of eYFP (green) and mCherry (red) in the CeM. Scale bar, 100  $\mu$ m. **f**, Representative image showing mCherry<sup>+</sup> terminals in PAG subregions. Scale bar, 200  $\mu$ m. **g**, Morphometric analysis showing that IPAG contains a significantly greater density of mCherry<sup>+</sup> terminals ( $n = 3$  mice; repeated-measures one-way ANOVA,  $F_{2,36} = 12.50$ ,  $P = 0.0006$ ; Bonferroni's multiple comparison test). Box and whisker plots indicate median and interquartile range, and crosses indicate means. **h**, Schematic of targeting and recording strategy. **i**, Representative tracings of evoked synaptic responses in dIPAG- or IPAG-projecting (top) and vIPAG-projecting (bottom) CeM cells by photostimulation of DP axonal fibres in absence (black line) and presence of 4-aminopyridine (4AP) and tetrodotoxin (TTX) application (grey line). Blue line indicates the onset of LED. **j**, Amplitude of evoked monosynaptic excitatory postsynaptic currents was significantly higher in dIPAG- or IPAG-projecting ( $n = 16$  cells from 10 mice) as compared to vIPAG-projecting ( $n = 13$  cells from 7 mice) CeM neurons (Mann–Whitney test,  $*P = 0.0367$ ). Data are presented as mean  $\pm$  s.e.m. **k**, Proportion of CeM neurons with evoked excitatory postsynaptic currents, classified by their projection target. Two-sided statistical tests were used. \*\* $P < 0.01$ , \* $P < 0.05$ .

terminals in the CeM elicits positive valence behaviour whereas excitation of VGLUT2<sup>+</sup> terminals elicits avoidance and flight. Our electrophysiology data suggest that the effects on flight are mediated through DP-mediated excitation of CeM neurons projecting to the PAG. How the VGLUT1<sup>+</sup> DP population exerts its appetitive effects in the CeM is still to be determined (Supplementary Discussion).

Collectively, the finding of this study add to a growing body of literature defining the CeA as a vital limbic brain structure that integrates complex sensory information to generate survival behaviour<sup>23,31–33</sup>. It has been demonstrated that CeL circuit activity is regulated by local recurrent inhibitory interactions<sup>23,34,35</sup>, and this mutual inhibition motif is important for rapid action selection. Future studies should investigate whether a similar ‘winner-take-all’ motif is used in the CeM to select between freezing versus flight responses.

CeM output neurons control freezing through projections to the PAG<sup>28,36,37</sup>, and our results demonstrate that the CeM is also important for flight. We found that DP-to-CeA projections target specific classes of CeM neurons that project to regions of the PAG traditionally implicated in flight<sup>26</sup>, with weaker VGLUT2<sup>+</sup> inputs to the vIPAG, which is linked to freezing<sup>28</sup>. It should be noted that the IPAG can elicit both freezing and flight, and defensive action selection in this region depends on numerous factors, including stimulation strength and neuronal identity<sup>38–40</sup>. The current study supports the idea that top-down integration of information in the IPAG from the DP-to-CeM pathway contributes to defensive action selection to threat<sup>41,42</sup>. How this circuit ultimately influences PAG circuits to induce flight should be a topic of future investigation.

Learned fear is traditionally assayed using freezing, control of which involves the well-established mPFC–basolateral amygdala–CeA pathway<sup>43</sup>. Previous research has shown that infralimbic projections to the basolateral amygdala and intercalated cell masses effectively operate to inhibit fear by supporting fear extinction<sup>44,45</sup>. By contrast, the DP-to-CeA pathway defined here operates under high-threat conditions and is necessary for generating flight. The context and cue specificity of DP-to-CeA activation and function is consistent with the known role of context and salience in defensive action selection<sup>46–48</sup>. Our findings therefore implicate the importance of the mPFC in executive control over high-intensity fear responses and may lead to a better understanding of the cortical dysfunction observed in post-traumatic stress disorder and panic disorder<sup>14</sup>.

## Online content

Any methods, additional references, Nature Portfolio reporting summaries, source data, extended data, supplementary information, acknowledgements, peer review information; details of author contributions and competing interests; and statements of data and code availability are available at <https://doi.org/10.1038/s41586-023-06912-w>.

1. Fonzo, G. A. et al. PTSD psychotherapy outcome predicted by brain activation during emotional reactivity and regulation. *Am. J. Psychiatry* **174**, 1163–1174 (2017).
2. Fadok, J. P. et al. A competitive inhibitory circuit for selection of active and passive fear responses. *Nature* **542**, 96–99 (2017).
3. Roelofs, K. Freeze for action: neurobiological mechanisms in animal and human freezing. *Philos. Trans. R. Soc. B* **372** (2017).
4. Fanselow, M. S., Hoffman, A. N. & Zhuravka, I. Timing and the transition between modes in the defensive behavior system. *Behav. Processes* **166**, 103890 (2019).
5. Blanchard, D. C. & Blanchard, R. J. Defensive behaviors, fear, and anxiety. in *Handbook of Anxiety and Fear* (eds Blanchard, R. J. et al.) 63–79 (Elsevier, 2008).
6. Perusini, J. N. & Fanselow, M. S. Neurobehavioral perspectives on the distinction between fear and anxiety. *Learn. Mem.* **22**, 417–425 (2015).
7. Johnson, P. L., Truitt, W. A., Fitz, S. D., Lowry, C. A. & Shekhar, A. Neural pathways underlying lactate-induced panic. *Neuropsychopharmacology* **33**, 2093–2107 (2008).
8. Münsterkötter, A. L. et al. Spider or no spider? Neural correlates of sustained and phasic fear in spider phobia. *Depress. Anxiety* **32**, 656–663 (2015).
9. Mobbs, D. et al. From threat to fear: the neural organization of defensive fear systems in humans. *J. Neurosci.* **29**, 12236–12243 (2009).
10. Tromp, D. P. M. et al. Reduced structural connectivity of a major frontolimbic pathway in generalized anxiety disorder. *Arch. Gen. Psychiatry* **69**, 925–934 (2012).
11. Marek, R., Strobel, C., Bredy, T. W. & Sah, P. The amygdala and medial prefrontal cortex: partners in the fear circuit. *J. Physiol.* **591**, 2381–2391 (2013).
12. Senn, V. et al. Long-range connectivity defines behavioral specificity of amygdala neurons. *Neuron* **81**, 428–437 (2014).
13. Karalis, N. et al. 4-Hz oscillations synchronize prefrontal–amygdala circuits during fear behavior. *Nat. Neurosci.* **19**, 605–612 (2016).
14. Andrewes, D. G. & Jenkins, L. M. The role of the amygdala and the ventromedial prefrontal cortex in emotional regulation: implications for post-traumatic stress disorder. *Neuropsychol. Rev.* **29**, 220–243 (2019).
15. De Franceschi, G., Vivattanasarn, T., Saleem, A. B. & Solomon, S. G. Vision guides selection of freeze or flight defense strategies in mice. *Curr. Biol.* **26**, 2150–2154 (2016).
16. Wang, W. et al. Coordination of escape and spatial navigation circuits orchestrates versatile flight from threats. *Neuron* **109**, 1848–1860 (2021).
17. McDonald, A. J. Cortical pathways to the mammalian amygdala. *Prog. Neurobiol.* **55**, 257–332 (1998).
18. Kataoka, N., Shima, Y., Nakajima, K. & Nakamura, K. A central master driver of psychosocial stress responses in the rat. *Science* **367**, 1105–1112 (2020).
19. Anastasiades, P. G. & Carter, A. G. Circuit organization of the rodent medial prefrontal cortex. *Trends Neurosci.* **44**, 550–563 (2021).
20. Fremeau, R. T. et al. The expression of vesicular glutamate transporters defines two classes of excitatory synapse. *Neuron* **31**, 247–260 (2001).
21. Borkar, C. D. & Fadok, J. P. A novel Pavlovian fear conditioning paradigm to study freezing and flight behavior. *J. Vis. Exp.* <https://doi.org/10.3791/61536> (2021).
22. Anderson, D. J. & Adolphs, R. A framework for studying emotions across species. *Cell* **157**, 187–200 (2014).
23. Fadok, J. P., Markovic, M., Tovote, P. & Lüthi, A. New perspectives on central amygdala function. *Curr. Opin. Neurobiol.* **49**, 141–147 (2018).
24. Dumont, É. C., Martina, M., Samson, R. D., Drolet, G. & Paré, D. Physiological properties of central amygdala neurons: species differences. *Eur. J. Neurosci.* **15**, 545–552 (2002).
25. Duvarci, S., Popa, D. & Paré, D. Central amygdala activity during fear conditioning. *J. Neurosci.* **31**, 289–294 (2011).
26. Li, J. N. & Sheets, P. L. The central amygdala to periaqueductal gray pathway comprises intrinsically distinct neurons differentially affected in a model of inflammatory pain. *J. Physiol.* **596**, 6289–6305 (2018).
27. Rizvi, T. A., Ennis, M., Behbehani, M. M. & Shipley, M. T. Connections between the central nucleus of the amygdala and the midbrain periaqueductal gray: topography and reciprocity. *J. Comp. Neurol.* **303**, 121–131 (1991).
28. Tovote, P. et al. Midbrain circuits for defensive behaviour. *Nature* **534**, 206–212 (2016).
29. Bandler, R. & Carrive, P. Integrated defence reaction elicited by excitatory amino acid microinjection in the midbrain periaqueductal grey region of the unrestrained cat. *Brain Res.* **439**, 95–106 (1988).
30. Behbehani, M. M. Functional characteristics of the midbrain periaqueductal gray. *Prog. Neurobiol.* **46**, 575–605 (1995).
31. Keifer, O. P., Hurt, R. C., Ressler, K. J. & Marvar, P. J. The physiology of fear: reconceptualizing the role of the central amygdala in fear learning. *Physiology* **30**, 389–401 (2015).
32. Ressler, R. L. & Maren, S. Synaptic encoding of fear memories in the amygdala. *Curr. Opin. Neurobiol.* **54**, 54–59 (2019).
33. Kong, M. S. & Zweifel, L. S. Central amygdala circuits in valence and salience processing. *Behav. Brain Res.* **410**, 113355 (2021).
34. Li, H. et al. Experience-dependent modification of a central amygdala fear circuit. *Nat. Neurosci.* **16**, 332–339 (2013).
35. Hunt, S., Sun, Y., Kucukdereli, H., Klein, R. & Sah, P. Intrinsic circuits in the CeL. *eNeuro* **4**, e0367-16.2017 (2017).
36. Viviani, D. et al. Oxytocin selectively gates fear responses through distinct outputs from the central amygdala. *Science* **333**, 104–107 (2011).
37. Massi, L. et al. Disynaptic specificity of serial information flow for conditioned fear. *Sci. Adv.* **9**, eabq1637 (2023).
38. Assareh, N., Sarrami, M., Carrive, P. & McNally, G. P. The organization of defensive behavior elicited by optogenetic excitation of rat lateral or ventrolateral periaqueductal gray. *Behav. Neurosci.* **130**, 406–414 (2016).
39. Yu, H. et al. Periaqueductal gray neurons encode the sequential motor program in hunting behavior of mice. *Nat. Commun.* **12**, 6523 (2021).
40. La-Vu, M. Q. et al. Sparse genetically defined neurons refine the canonical role of periaqueductal gray columnar organization. *Elife* **11**, e77115 (2022).
41. Evans, D. A. et al. A synaptic threshold mechanism for computing escape decisions. *Nature* **558**, 46–76 (2009).
42. Wang, W. et al. Dorsal premammillary projection to periaqueductal gray controls escape vigor from innate and conditioned threats. *Elife* **10**, e69178 (2021).
43. Tovote, P., Fadok, J. P. & Lüthi, A. Neuronal circuits for fear and anxiety. *Nat. Rev. Neurosci.* **16**, 317–331 (2015).
44. Quirk, G. J., Likhtik, E., Pelletier, J. G. & Paré, D. Stimulation of medial prefrontal cortex decreases the responsiveness of central amygdala output neurons. *J. Neurosci.* **23**, 8800–8807 (2003).
45. Bukalo, O. et al. Prefrontal inputs to the amygdala instruct fear extinction memory formation. *Sci. Adv.* **1**, e1500251 (2015).
46. Hersman, S., Allen, D., Hashimoto, M., Brito, S. I. & Anthony, T. E. Stimulus salience determines defensive behaviors elicited by aversively conditioned serial compound auditory stimuli. *Elife* **9**, e53803 (2020).
47. Dong, P. et al. A novel cortico-intrathalamic circuit for flight behavior. *Nat. Neurosci.* **22**, 941–949 (2019).
48. Totty, M. S. et al. Behavioral and brain mechanisms mediating conditioned flight behavior in rats. *Sci. Rep.* **11**, 8215 (2021).

**Publisher's note** Springer Nature remains neutral with regard to jurisdictional claims in published maps and institutional affiliations.

Springer Nature or its licensor (e.g. a society or other partner) holds exclusive rights to this article under a publishing agreement with the author(s) or other rightsholder(s); author self-archiving of the accepted manuscript version of this article is solely governed by the terms of such publishing agreement and applicable law.

© The Author(s), under exclusive licence to Springer Nature Limited 2024

# Article

## Methods

### Animals

Male and female C57BL/6J (stock number 000664, Jackson Laboratories), CRH-IRES-Cre (stock number 012704), SOM-IRES-Cre (stock number 013044), VGLUT1-IRES-Cre (Slc17a7-IRES2-Cre-D, stock number 023527) and VGLUT2-IRES-Cre (stock number 028863) mice aged 5–12 weeks were used. All Cre-driver lines were fully backcrossed to C57BL/6J. Mice were individually housed on a 12-h light/dark cycle with ad libitum food and water (average room temperature 70–72 °F; humidity, 50–60%). Behavioural experiments were carried out during the light phase. Implanted animals were habituated to handling by cupping the mouse in hand for 5 min per day for 2 days before the start of the experiment. All animal procedures were carried out following institutional guidelines and were approved by the Tulane University Institutional Animal Care and Use Committee.

### Viral vectors

For optogenetic experiments, we used AAV5-EF1a-DIO-hChR2(H134 R)-eYFP-WPRE-HGHPa (Addgene 20298), AAV5-hSyn-hChr2(H134R)-mCherry (Addgene 26976), AAV5-EF1a-DIO-eNpHR3.0-eYFP (Addgene 26966) and AAV5-EF1a-DIO-eYFP (Addgene 27056; all gifts from Karl Deisseroth). For chemogenetics, we used AAV5-hSyn-DIO-hM3D(Gq)-mCherry (Addgene 44361), AAV-hSyn-DIO-hM4D(Gi)-mCherry (Addgene 44362) and AAV5-hSyn-DIO-mCherry (Addgene 50459; all gifts from Bryan Roth). For Cre-dependent GCaMP6f expression, we used AAV5-CAG-Flex-GcaMP6f-WPRE-SV40 (Addgene 100835, a gift from Douglas Kim and GENIE Project). To retrogradely express Cre, we used CAV2-Cre (PVM)<sup>49</sup>. For neuronal tracing and cell labelling experiments, we used AAV5-hSyn-DIO-mCherry (Addgene 50459, a gift from Bryan Roth), AAV5-EF1a-DIO-eYFP (Addgene 27056, a gift from Karl Deisseroth) and pENN-AAV1.hSyn.HI.eGFP-Cre-WPRE.SV40 (Addgene 105540, a gift from James M. Wilson).

### Surgery

Mice were deeply anaesthetized using 5% isoflurane (Fluriso, VetOne) in oxygen-enriched air (OxyVet O<sub>2</sub> Concentrator, Vetequip), followed by a subcutaneous injection of 2 mg kg<sup>-1</sup> meloxicam (OstiLox, VetOne), and then fixed into a stereotaxic frame (Model 900, Kopf Instruments) equipped with a robotic stereotaxic targeting system (Neurostar). Anaesthetized mice were maintained on 2–2.5% isoflurane, and a core body temperature was maintained at 36 °C using a feedback-controlled d.c. temperature controller (ATC2000, World Precision Instruments). Eye ointment (GenTeal) was applied to prevent dryness. The head was shaved, and the skin was sterilized using betadine iodine solution (Purdue Products). Then, 2% lidocaine (0.1 ml, lidocaine 2%, VetOne) was injected subcutaneously at the site of incision, and a midline incision was made with a scalpel to expose the skull.

**Injections.** For retrograde neuronal tracings, retrogradely transported beads (0.2 µl, 1:2 diluted with saline, Lumafluor) were stereotactically injected. For viral vectors, approximately 0.4 µl per hemisphere was injected bilaterally using pulled glass pipettes (tip diameter 10–20 µm, PC-100 puller), connected to a pressure ejector (PDES-Pressure Application System, npi electronic equipment).

The CeA coordinates used were: 1.2–1.3 mm posterior to bregma, ±2.8–2.9 mm lateral to the midline and 4.1–4.3 mm below the dura. The DP coordinates used were 1.8–1.9 mm anterior to bregma, ±0.4–0.5 mm lateral to the midline and 3.1–3.2 mm below the dura. The DMH coordinates used were 1.7 mm posterior to bregma, ±0.5 mm lateral to the midline and 5 mm below the dura. The dIPAG or IPAG and vIPAG coordinates used were –4.16 mm (–4.72 mm for vIPAG) posterior to bregma, –0.4 mm lateral to the midline and 2.4 mm (2.7 mm for vIPAG) below the dura.

**Fibre implantation for optogenetics.** Animals were bilaterally implanted with LC optic fibre stubs (fibre: 0.48 NA, 200–230 µm diameter, 6 mm length, Plexon) 2–3 weeks after viral vector injection. Optic fibre tips were lowered to 100–200 µm above the CeA. Implants were fixed to the skull with two miniature screws (00.90-100-M-SS-FH, US Micro Screw), cyanoacrylate glue gel (SuperGlue) and dental cement (Ortho-Jet powder and black liquid acrylate, Lang). Experiments were conducted 4 weeks after viral infections, to ensure adequate opsin expression.

**Lens implantation for Ca<sup>2+</sup> imaging.** Gradient index lens implantation surgery was carried out as described previously<sup>50,51</sup>. Mice were head fixed on the stereotaxic apparatus and a craniotomy was drilled over the DP coordinates, using a 1.2-mm-diameter round drill burr (Harvard Apparatus). Three additional holes were drilled to implant stainless steel screws (US Micro Screw, 00.90-100-M-SS-FH). The skull surface was cleaned of bone fragments and wiped using sterilized cotton tips. We aspirated the overlying tissue up to 1–1.5 mm above the site of implantation with a bent 27-gauge needle (NE-4527, Component Supply) with intermittent sterile saline washes. A gradient index lens (1 mm diameter, 9 mm length, 0.5 NA, 1 pitch, part number 1050-002177, Inskopix) was attached to the stereotaxic arm using a custom-built lens holder, and lowered for 3 mm over the course of 10 min. Kwik-Sil (World Precision Instruments) was used to fill in the gap between the lens and the skull and left to dry for 5 min. An adhesive cement (C&B S399 Metabond Quick Adhesive Cement System Parkell) mixed with liquid polymer (Catalyst + Quick Base) was applied around the lens over the skull and screws and allowed to dry. The lens holder was carefully detached from the lens. Layers of dental cement mixed with black acrylate (Ortho-Jet powder and black liquid acrylate) were applied around the lens to build the circular ridge of about 0.5 mm high below the top of the lens, and a thick layer of Kwik-cast (World Precision Instruments) was applied over the lens. Animals were then individually housed and allowed to recover for 2–3 weeks.

**Baseplating and verification of Ca<sup>2+</sup> transients.** Mice were checked weekly for GCaMP6f fluorescence and Ca<sup>2+</sup> transient activity after lens implantation, as previously described<sup>51</sup>. For baseplating, mice were anaesthetized with 5% isoflurane, fitted into the stereotaxic frame, and then maintained at 1%. A head-mounted miniscope (V4, UCLA open source, <http://miniscope.org/>) was fixed on a custom-built holder that was attached to the stereotaxic arm<sup>52</sup>. The focusing mechanism of the miniscope was set at mid-range. The coaxial cable from the miniscope was attached to the data acquisition box (DAQ-V3.2, UCLA), which was connected to the computer through USB 3.0. The baseplate was attached to the bottom of the miniscope and the miniscope objective lens was aligned over the relay lens. The recording software (Miniscope controller, UCLA) was turned on and the LED light intensity (25%), gain and frame rate (30 fps) were set. To ensure maximum field of view and focus on the centre of the lens, the miniscope tilt was adjusted to view all edges of the relay lens. Then, the miniscope was slowly moved in x, y and z planes to locate active cells or transients. If there were no transients, the mouse was returned to the home cage and checked again the following week.

If Ca<sup>2+</sup> transients were observed, they were further confirmed using tail pinch. If multiple cells were observed, then mice were baseplated. Dental cement mixed with black acrylate was applied layer-by-layer between the baseplate and the circular ridge built during lens implantation. The dental cement was applied so that no light could pass through from the outside. After the cement dried, the miniscope was detached and a plastic cover was installed to protect the relay lens.

### Miniscope recordings

Animals with Ca<sup>2+</sup> transients were subjected to the 4-day conditioned flight paradigm (described below). Data were continuously recorded at 30 frames s<sup>-1</sup>. Behaviour was simultaneously recorded to video ('Pike'

camera, Allied Vision). Only mice with flight responses were included in the Ca<sup>2+</sup> data analysis.

### Ca<sup>2+</sup> imaging processing

Ca<sup>2+</sup> imaging videos were concatenated using ImageJ software (<https://imagej.nih.gov/ij/download.html>). The concatenated videos were then processed using MATLAB and an open source analysis package (<https://bahanonu.github.io/ciatah/>) as described previously<sup>51,53</sup>. The videos were pre-processed by correcting for motion and temporally downsampled by a factor of six. After pre-processing the videos, we extracted individual neurons and their activity traces by using the open source package Constrained Nonnegative Matrix Factorization for microEndoscopic data ([https://github.com/zhoupc/CNMF\\_E](https://github.com/zhoupc/CNMF_E)). The extracted cells were then manually identified on the basis of the spatial filter and activity trace of each candidate cell along with the candidate cells' average Ca<sup>2+</sup> transient waveform. Data were averaged over a 200-ms sliding window. The data were normalized by calculating z scores (subtracting the mean activity score of the entire recording from each activity trace, divided by the standard deviation of each cell during the whole period) and the neurons with peaks that were  $\geq 3$  s.d. above baseline were considered as active neurons. To determine statistically significant changes in responses of the DP-to-CeA projection cells to the tone and WN, the z scores from the corresponding periods were averaged and compared. At the end of the experiments, animals were perfused and their brains were isolated to confirm lens placement. Only data from animals with correct lens placement were used for analysis.

### Behavioural paradigms

**Conditioned flight paradigm.** Two different contexts were used. Context A (low-threat context) consisted of a clear cylindrical chamber with a smooth floor, whereas context B (high-threat context) consisted of a square enclosure with an electrical grid floor used to deliver a.c. footshocks (ENV-414S, Med Associates). These two chambers were cleaned with 1% acetic acid and 70% ethanol, respectively. An overhead speaker (ENV-224AM, Med Associates) delivered auditory stimuli generated by a programmable audio generator (ANL-926, Med Associates, Inc.). Behavioural protocols were generated using MedPC software (Med Associates).

We used a 4-day conditioned flight paradigm, as described previously<sup>2,21</sup>. In brief, during preconditioning in context A, mice receive four presentations of a SCS consisting of a 10-s tone (7.5 kHz, 500-ms pips at 1 Hz, 75 dB) and a 10-s WN (random distribution of 1 to 20,000 Hz, 500-ms pips at 1 Hz, 75 dB). On days 2 and 3 in context B, mice are presented with five pairings of the SCS co-terminating with a 1-s, 0.9-mA footshock. During recall in context A (or context B for recall in the high-threat context group), mice were presented with four trials of the SCS without footshock.

**Quantification of defensive behaviour.** All sessions were recorded to video, and behaviour was analysed using contour tracking (Cineplex software, Plexon). Freezing was defined as a complete cessation of movement for at least 1 s and was automatically scored using a frame-by-frame analysis of pixel changes (Cineplex Editor, Plexon). Results were confirmed by a trained observer blinded to condition. By determining a calibration coefficient using the chambers' known size and the camera's pixel dimensions, speed (cm s<sup>-1</sup>) was extracted using the animal's centre of gravity<sup>21</sup>.

Escape jumping was scored manually from video files by a blinded observer. Flight scores were calculated by dividing the average speed during each compound stimulus (CS) by the average speed during the 10-s pre-CS from all of the trials (baseline (BL)) and then adding 1 point for each escape jump (speedCS/speedBL + number of jumps). The flight score is therefore a combined score of forward bursts of speed (darting) and escape jumping behaviour. A flight score of 1 indicates no change in flight behaviour from the preSCS period.

**OFT.** A 45 × 45 × 45 cm arena made of white opaque Plexiglas was used. The arena was cleaned using 70% ethanol after each mouse. Mouse behaviour was tracked under 100-lux light conditions using a top-mounted camera ('Pike' camera, Allied vision). For chemogenetic experiments, the OFT duration was 10 min. For optogenetic experiments, the OFT duration was 6 min. After a 120-s baseline period, four 30-s on-off trials of light stimulation were used. For eNpHR experiments, a continuous orange light was used at 10-mW power at the fibre tip, and for ChR2 experiments, 10-ms pulses of blue light were used at 20 Hz, and 10-mW power at the fibre tip.

The time spent in the inner zone, the number of entries into it, and total distance travelled were measured using tracking software (Cineplex Studio, Plexon).

**EPM.** Behaviour was tracked using a top-mounted camera ('Pike' camera, Allied Vision) for 10 min. The maze was made from white opaque Plexiglas material and consisted of four 30-cm long and 7-cm-wide arms. Two open arms had no walls, and two enclosed arms had 15-cm-high walls. The maze was elevated 40 cm above the ground. The arena was cleaned using 70% ethanol after every test. The total time spent in the open arms was calculated using Cineplex Editor software (Plexon).

### Chemogenetic manipulations of behaviour

Behavioural testing was carried out 3–4 weeks after viral injections. First, mice were subjected to the OFT. The next day, animals were subjected to the EPM. Thirty minutes before the start of behavioural testing, animals were injected with CNO (0.5 mg ml<sup>-1</sup> in vehicle (0.9% saline), given as 10 ml kg<sup>-1</sup> for final dose of 5 mg kg<sup>-1</sup>, intraperitoneally; Enzo Life Sciences) or vehicle (10 ml kg<sup>-1</sup> volume, ip).

### Optogenetic manipulations of behaviour

For optogenetic modulation, we used a Plex controller system (Plexon) operated through Radiant software (Plexon). Two PlexBright LED modules (Plexon) were connected to the controller, and an LC patch cable (200–230-μm fibre, 1 m long, 0.66 NA, Plexon) was connected. Laser power at the fibre tip was measured before every test with an optical power and energy meter (PM100D, ThorLabs). The patch cable was connected to the head-mounted fibre stubs using ceramic sleeves. Connectors were tested for coupling efficiency before implantations, and laser power at the fibre tip for behavioural manipulations was adjusted to reach a value of 10 mW.

Optogenetic inhibition experiments were carried out using a within-subjects design with eight trials during FC2 (day 3), with four pairs of alternating trials of light on and off (counter-balanced). During recall (day 4), mice were presented with three pairs of alternating light on and off trials. On light trials, a 620-nm light was switched on 500 ms before the onset of the SCS (first tone pip) and remained on until the end of the last WN pip (20.5 s in total). For ChR2-induced excitation of DP-to-CeA neuronal populations (Extended Data Fig. 5), we used 465-nm light pulses (20 Hz, 10-ms width) that began 500 ms before the onset of the SCS (first tone pip) and remained on until the end of the last WN pip (20.5 s in total). For ChR2 manipulation during lower footshock intensity (0.68 mA) groups (Extended Data Figs. 6–8), light pulses were delivered with the first WN pip and remained on until the end of 10-s post-cue periods (20.5 s in total). For optogenetic excitation and control experiments, the mice were presented with five trials on day 3 with two pairs of alternating light on and off trials (counter-balanced). During recall, mice were presented with two pairs of alternating light on and off trials (counter-balanced). For recall in the high-threat context, we presented mice with five trials, all light on.

### Real-time place aversion test

We used a custom-made 50 × 50 × 50 cm arena made from white opaque Plexiglas and divided into two equal compartments. One side of the chamber was allotted as the stimulation side and other as a neutral side

# Article

(non-stimulated, with striped walls and metallic plate floor). Mice were placed in the non-stimulated side, and 20-Hz blue LED light stimulation was delivered each time the mouse moved to the stimulation side of the chamber. The light stimulation was continuously on until the mouse moved back into the non-stimulation compartment. The session lasted 10 min and was recorded using a top-mounted recording camera attached to recording system (Plexon) and scored using Cineplex editor (Plexon) by a blinded experimenter. The percentage of time spent in the stimulation chamber was used as a measure of aversion.

## Immunohistochemistry

Following the completion of experiments, mice were anaesthetized with tribromoethanol (240 mg kg<sup>-1</sup>) and perfused transcardially with phosphate-buffered saline (PBS) followed by 4% paraformaldehyde in PBS. Brains were isolated and stored in paraformaldehyde overnight. The next day, fixed brains were sectioned using a vibrating microtome (Precisionary) in 60-μm-thick (for Fos immunohistochemistry) or 80-μm-thick coronal slices.

Antibody staining was carried out on floating tissue sections. Briefly, sections were washed in PBS-Triton X-100 (PBST, 0.3%) and blocked using 5% goat serum in PBST for 1 h followed by an overnight (for RFP or GFP staining), or 48-h (for Fos staining) incubation in primary antibodies at 4 °C. Primary antibodies used in this study were rabbit anti-RFP (1:1,500, 600-401-379, Rockland Immunochemicals), chicken anti-GFP (1:2,000, NB100-1614, Novus Biologicals) and rabbit anti-Fos (1:1,000, 226003, Synaptic Systems). After primary antibody incubation, sections were washed in PBST and incubated in secondary antibodies in PBST (1:500 donkey anti-rabbit AlexaFluor 555 (catalogue number A31572) and goat anti-rabbit AlexaFluor 488 (catalogue number A11034) or goat anti-chicken AlexaFluor 488 (catalogue number A-11039), Thermo Fisher Scientific). Following final rinses with PBS, sections were mounted and scanned from the DP and CeA.

Images were obtained using an Axio Scan.Z1 slide-scanning microscope (Zeiss) and a confocal microscope (FV3000, Olympus). Mice were included in subsequent data analyses only if bilateral expression specific to the target region was observed.

## Fos quantification

Red fluorescent retro-beads were injected into the CeA of C57BL/6J mice. Seven days later, animals were divided into four groups: home cage control, shock only, SCS-FC and unpaired. Shock only, unpaired and SCS-FC mice were subjected to 2 days of conditioning and were killed 90 min after the second session by transcardial perfusion. Following brain sectioning and immunohistochemical staining for Fos, confocal images were taken. The quantification of Fos<sup>+</sup>, bead-positive and cells with both markers was carried out by a blinded observer using ImageJ.

## Brain slice electrophysiology

**Slice preparation.** Coronal brain slices containing the CeA were collected from mice at least 2 weeks after viral injections for ex vivo electrophysiological recordings, as described earlier<sup>35,54</sup>. Mice (9+ weeks) were anaesthetized with tribromoethanol and transcardially perfused with ice-cold solution containing (in mM): 93 N-methyl-D-glucoside, 2.5 KCl, 30 NaHCO<sub>3</sub>, 0.5 CaCl<sub>2</sub>, 10 MgSO<sub>4</sub>, 1.2 NaH<sub>2</sub>PO<sub>4</sub>, 20 HEPES, 25 glucose, 5 Na ascorbate, 3 Na pyruvate, 2 thiourea. Brains were dissected and 300-μm slices were prepared with a vibratome (Leica Microsystems) and maintained in oxygenated recording artificial cerebrospinal fluid containing (in mM): 126 NaCl, 2.5 KCl, 1.25 NaH<sub>2</sub>PO<sub>4</sub>, 1.3 MgCl<sub>2</sub>, 2.5 CaCl<sub>2</sub>, 26 NaHCO<sub>3</sub> and 10 glucose at 34 °C for 30 min before decreasing the chamber temperature to about 20 °C.

**Patch clamp recording.** Slices were transferred to a submerged recording chamber mounted on the fixed stage of an Olympus BX51WI fluorescence microscope, visualized with differential interference contrast illumination, and continuously perfused with warmed

(32 °C) oxygenated artificial cerebrospinal fluid at a rate of 2 ml min<sup>-1</sup>. Whole-cell patch clamp recordings were carried out in eYFP-labelled SOM<sup>+</sup> or CRH<sup>+</sup> neurons, retrolabelled neurons (1:10 diluted beads from dIPAG or IPAG, or vIPAG) or unlabelled neurons in the CeM or CeL. Borosilicate glass pipettes with a resistance of 3–5 MΩ were filled with intracellular patch solution containing (in mM): 130 potassium gluconate, 10 HEPES, 10 phosphocreatine Na<sub>2</sub>, 4 Mg ATP, 0.4 Na GTP, 5 KCl, 0.6 EGTA; pH was adjusted to 7.25 with KOH and the solution had a final osmolarity of about 290 mOsm. Series resistance was below 15 MΩ immediately after break-in, and cells were discarded if it exceeded 30 MΩ. An optical fibre was placed approximately 2 mm above the slice and ChR2-expressing DP fibres were stimulated by 465-nm LED illumination (single 10-ms pulses, 15 mW power, delivered at 1 Hz). excitatory postsynaptic current sensitivity to DNQX (20 μM) was confirmed where indicated.

To assess firing properties in CeA neurons that exhibited fast synaptic responses, 500–750-ms depolarizing current injections were applied in current clamp mode. To compare the properties of monosynaptic excitatory postsynaptic currents evoked by optogenetic stimulation of DP fibres, responses were recorded in the presence of 1 mM 4-aminopyridine and 1 μM tetrodotoxin. Data were acquired using a Multiclamp 700B amplifier, a Digidata 1440A analog–digital interface and pClamp 10 software (Molecular Devices). Recordings were filtered at 4 kHz and sampled at 20 kHz. Data were analysed with Clampfit 10 (Molecular Devices). Statistical comparisons were conducted with a paired or unpaired Student's *t*-test (*P*<0.05 with a two-tailed analysis was considered significant).

## Statistics and reproducibility

Data were analysed for statistical significance using Prism 10 (GraphPad Software). Statistical significance was set at *P*<0.05. Data were tested for normal distribution using the Shapiro–Wilk normality test ( $\alpha=0.05$ ). For pairwise comparisons, the appropriate parametric (unpaired Student's *t*-test) or non-parametric (Mann–Whitney test and Wilcoxon matched-pairs signed rank) test was carried out. Data with more than two study groups were analysed using one-way ANOVA followed by Bonferroni's post hoc tests. For calcium imaging data analysis, we used custom code written in MATLAB. Correlations analysis and plotting regression lines were carried out using GraphPad Prism 10. The sample size was determined on the basis of previously published research.

For the representative images presented in the figures, the total number of replications is as follows: Fig. 1b,c, *n*=6 mice; Fig. 1f,h, *n*=5 mice; Fig. 1g,h, *n*=6 mice; Fig. 1l–m, *n*=6 mice; Fig. 2c, *n*=6 mice; Fig. 3b, *n*=40 mice; Fig. 4c, *n*=18 mice; Fig. 5e,f, *n*=3 mice; Extended Data Fig. 9b, *n*=3 mice; Extended Data Fig. 10, *n*=3 mice.

## Reporting summary

Further information on research design is available in the Nature Portfolio Reporting Summary linked to this article.

## Data availability

All data supporting the findings of this study are available within the paper and its Supplementary Information. Source data are provided with this paper.

49. Soudais, C., Laplace-Builhe, C., Kiss, K. & Kremer, E. J. Preferential transduction of neurons by canine adenovirus vectors and their efficient retrograde transport *in vivo*. *FASEB J.* **15**, 2283–2285 (2001).
50. Resende, S. L. et al. Visualization of cortical, subcortical and deep brain neural circuit dynamics during naturalistic mammalian behavior with head-mounted microscopes and chronically implanted lenses. *Nat. Protoc.* **11**, 566–597 (2016).
51. Corder, G. et al. An amygdalar neural ensemble that encodes the unpleasantness of pain. *Science* **363**, 276–281 (2019).
52. Ghosh, K. K. et al. Miniaturized integration of a fluorescence microscope. *Nat. Methods* **8**, 871–878 (2011).
53. Parker, J. G. et al. Diametric neural ensemble dynamics in parkinsonian and dyskinetic states. *Nature* **557**, 177–182 (2018).

54. Chen, C. et al. Astrocytes amplify neuronal dendritic volume transmission stimulated by norepinephrine. *Cell Rep.* **29**, 4349–4361 (2019).

**Acknowledgements** We thank B. Ahanonu for providing MATLAB codes and assistance with calcium imaging data analysis; and R. Mostany and S. Yun for help in standardization of calcium imaging and data analysis. This work was supported by the Louisiana Board of Regents through the Board of Regents support fund (LEQSF(2018-21)-RD-A-17) to J.P.F., the National Institute of Mental Health of the National Institutes of Health under award numbers R01MH122561 to J.P.F. and R01MH119283 to J.G.T., and the National Institute of Neurological Disorders and Stroke of the National Institutes of Health under award number R01NS122840 to J.G.P. The content is solely the responsibility of the authors and does not necessarily represent the official views of the National Institutes of Health.

**Author contributions** Conceptualization—C.D.B. and J.P.F.; formal analysis—C.D.B., C.E.S., X.F., M.D., Q.-S.E.L., R.V., C.V., A.W., S.B., A.D., E.B., A.R., J.G.P. and J.P.F.; funding acquisition—J.P.F.;

investigation—C.D.B., C.E.S., X.F. and Q.-S.E.L.; methodology—C.D.B., M.D., C.E.S., J.G.T. and J.P.F.; project administration and supervision—C.D.B., J.P.F. and J.G.T.; resources—J.P.F. and J.G.T.; visualization—C.D.B., C.E.S., M.D., X.F. and J.P.F.; writing, original draft—C.D.B. and J.P.F.; writing, review and editing—C.D.B., C.E.S., X.F., J.G.T., J.G.P. and J.P.F.

**Competing interests** The authors declare no competing interests.

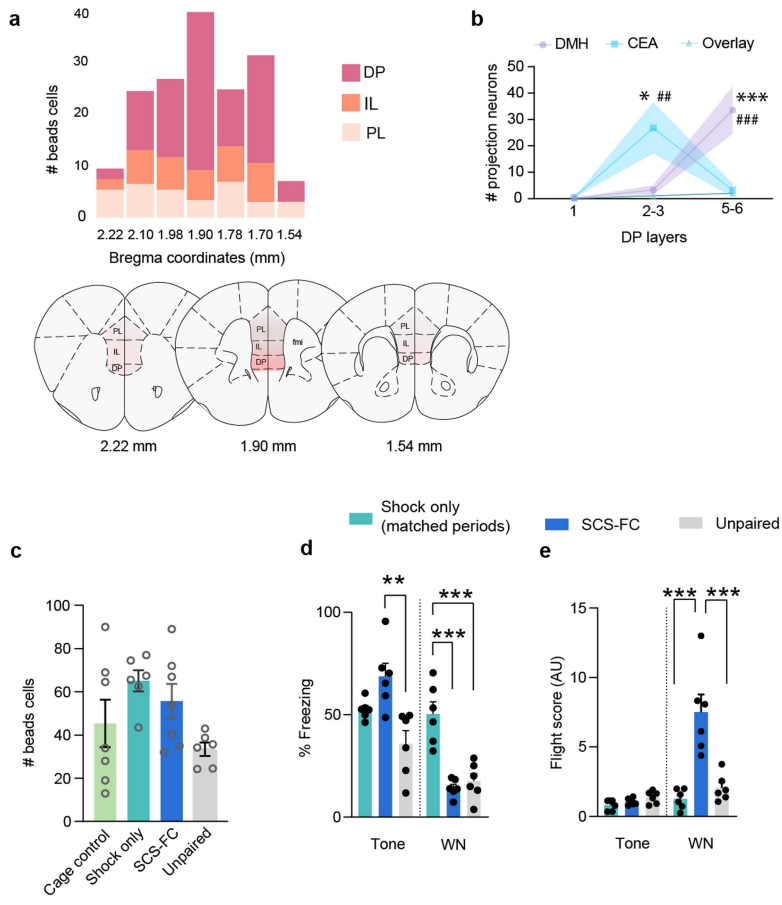
**Additional information**

**Supplementary information** The online version contains supplementary material available at <https://doi.org/10.1038/s41586-023-06912-w>.

**Correspondence and requests for materials** should be addressed to Jonathan P. Fadok.

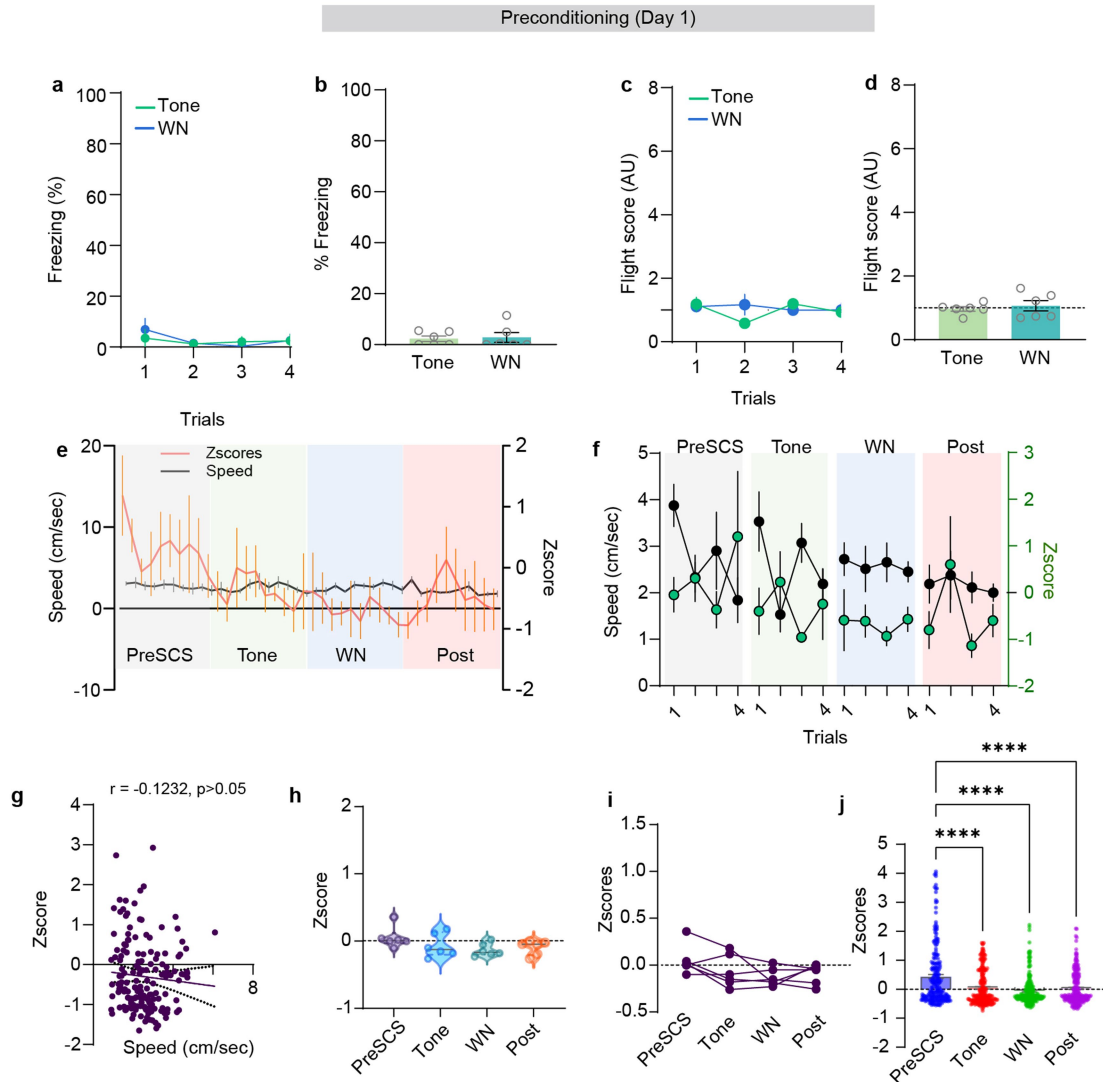
**Peer review information** *Nature* thanks Avishek Adhikari, Larry Zweifel and the other, anonymous, reviewer(s) for their contribution to the peer review of this work. Peer reviewer reports are available.

**Reprints and permissions information** is available at <http://www.nature.com/reprints>.



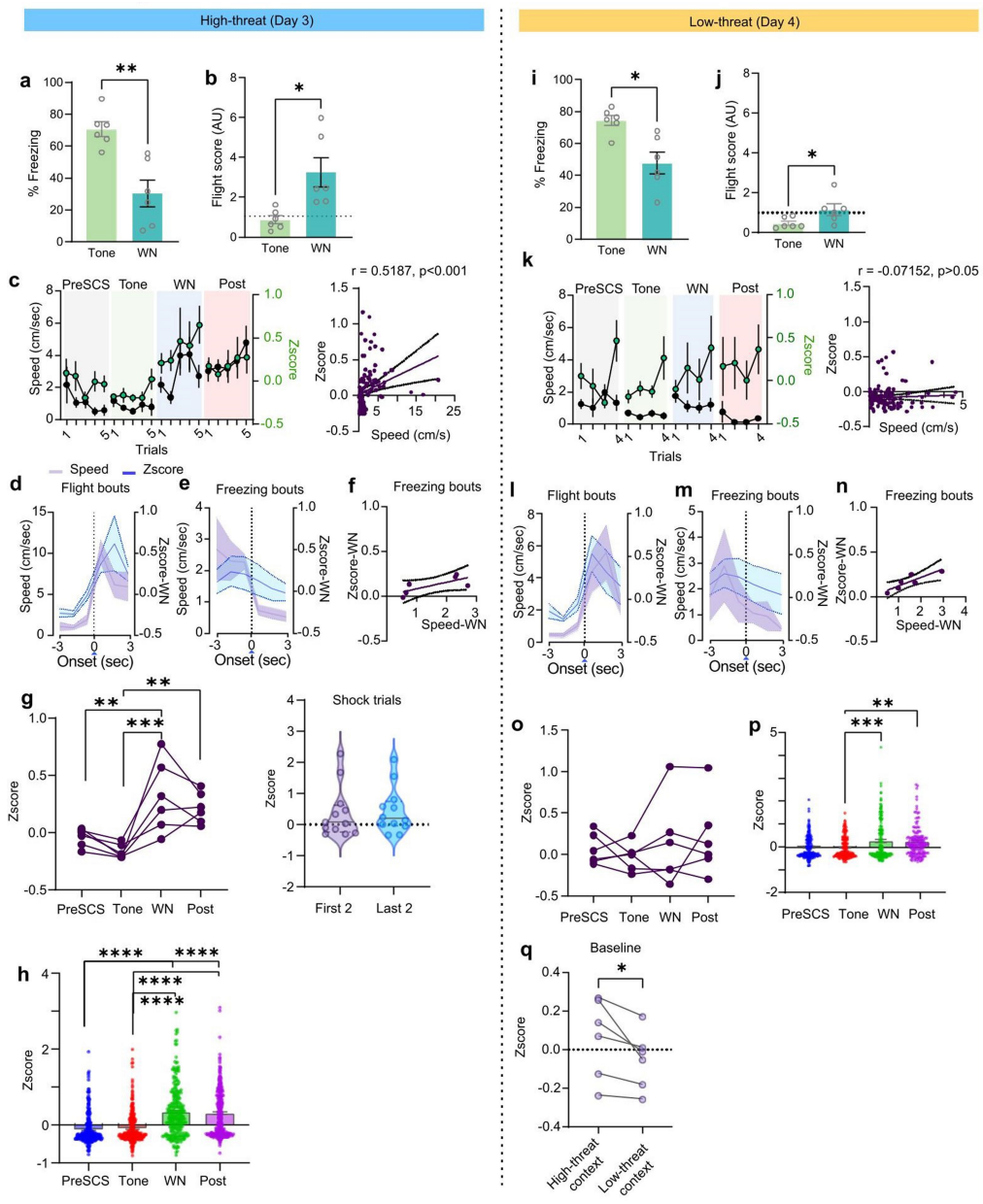
**Extended Data Fig. 1 | (Data related to Fig. 1): Neuroanatomy of the DP-CeA pathway.** **a**, Top, Number of CeA-projecting mPFC cells across the antero-posterior axis. Bottom, Schematic of coronal sections showing the density of beads in DP on antero-posterior scale. The coronal sections were adapted from the Allen Brain Atlas (Allen Institute for Brain Science). **b**, The layer-wise distribution of bead+ cells in the DP that project to CeA and/or DMH (N = 6 mice; two-way ANOVA, layer x group,  $F_{(4,45)} = 10.15, p < 0.0001$ ; Bonferroni's post-hoc test, \* $p < 0.05$ , \*\* $p < 0.001$  (DMH vs CeA), # $p < 0.01$ , ## $p < 0.001$  (vs

overlay). **c**, Total number of bead+ cells across groups (N = 6 mice per group; 3-4 slices per group; one-way ANOVA,  $F_{(3,22)} = 2.819, p = 0.0626$ ). **d**, Freezing of cFos groups on FC2 (N = 6 mice per group; one-way ANOVA for tone ( $F_{(2,15)} = 9.367, p = 0.0023$ ) and white noise (WN;  $F_{(2,15)} = 22.68, p < 0.0001$ ); Bonferroni's post-hoc test). **e**, Flight scores of cFos groups on FC2 (N = 6 mice per group; one-way ANOVA for tone ( $F_{(2,15)} = 3.60, p = 0.052$ ) and WN ( $F_{(2,15)} = 18.52, p < 0.0001$ ); Bonferroni's post-hoc test). Data in **b-e** represented as means ± s.e.m. Two-sided statistical tests were used. \*\*\* $P < 0.001$ , \*\* $P < 0.01$ .



**Extended Data Fig. 2 | (Data related to Fig. 2): Calcium imaging during pre-conditioning.** **a-b**, Trial-wise and average freezing of mice from calcium imaging experiments during preconditioning session ( $N = 6$  mice; paired t-test,  $t = 0.3051$ ,  $df = 5$ ,  $p = 0.77$ ). **c-d**, Trial-wise and average flight score of mice from calcium imaging experiments during preconditioning session ( $N = 6$  mice; paired t-test,  $t = 0.6565$ ,  $df = 5$ ,  $p = 0.54$ ). **e**, Speed and neuronal activity during the last trial of preconditioning session ( $n = 221$  cells from 6 mice). **f**, Average speed and neuronal activity during each trial of preSCS, tone, WN and post-cue periods ( $n = 221$  cells from 6 mice). **g**, Spearman correlation of speed and neuronal activity from all trials (10 s each epoch of preSCS, tone, WN and post

cue, each point represents one sec;  $n = 221$  cells from 6 mice;  $r = -0.1232$ , 95% CI:  $-0.2774$  to  $0.03724$ ,  $p = 0.12$ ). **h**, Average Z-score of the DP-to-CeA population during the preSCS, tone, WN and post-cue periods ( $n = 221$  cells from 6 mice; ordinary one-way ANOVA,  $F_{(3,20)} = 1.965$ ,  $p = 0.15$ ). **i**, Average Z-scores of individual mice during preSCS, tone, WN and post-cue periods ( $N = 6$  mice). **j**, Z-scores of individual neurons during the last trial of preconditioning ( $n = 221$  cells from 6 mice, one-way ANOVA,  $F_{(3,880)} = 21.43$ ,  $P < 0.0001$ ; Bonferroni's multiple comparisons test). Data in **a-f** and **j** represented as means  $\pm$  s.e.m. Violin plots in **h** indicate median, interquartile range, and the distribution of individual data points. Two-sided statistical tests were used. \*\*\*\* $p < 0.0001$ .

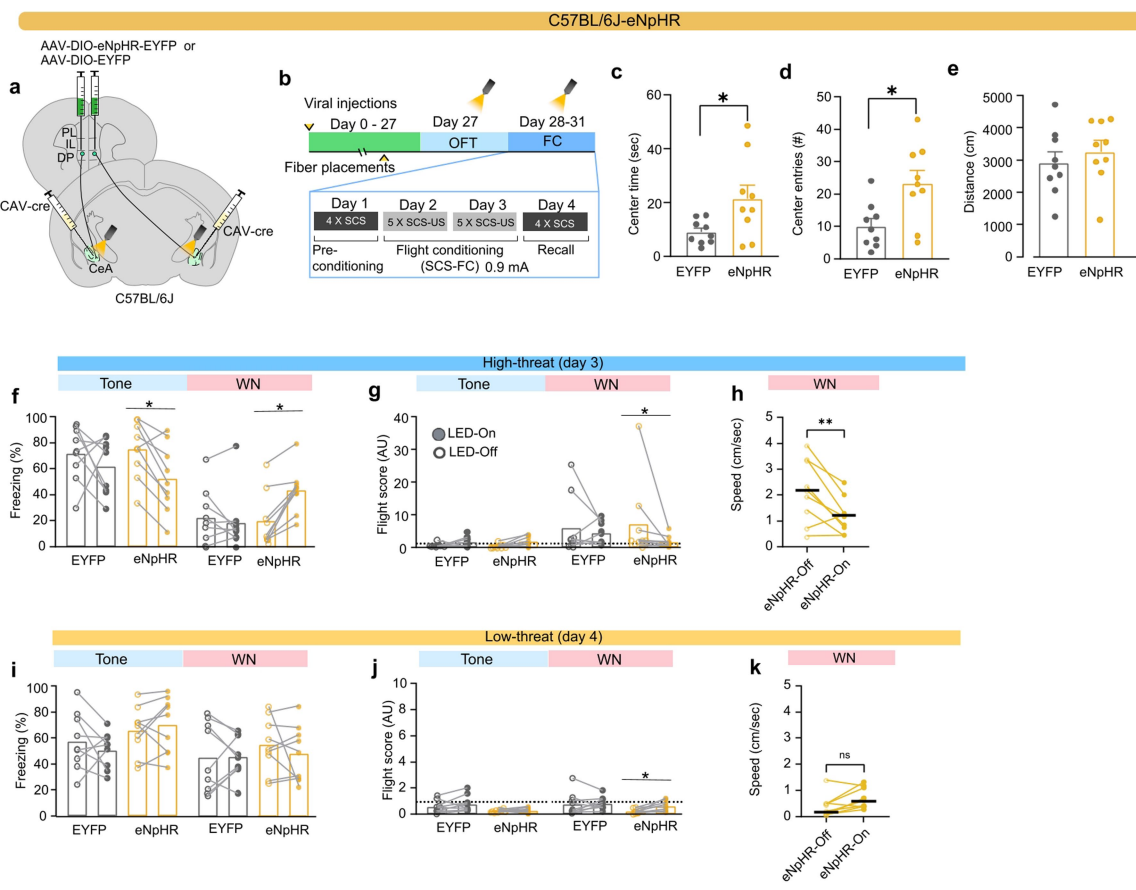


Extended Data Fig. 3 | See next page for caption.

**Extended Data Fig. 3 | (Data related to Fig. 2): Calcium imaging in the high-threat and low-threat contexts.** **a**, Freezing behaviour in the high-threat context (N = 6 mice; paired t-test,  $t = 4.744$ ,  $df=5$ ). **b**, Flight scores in the high-threat context. (N = 6 mice; paired t-test,  $t = 3.650$ ,  $df=5$ ). **c, left**, Average speed and neuronal activity during each trial of the preSCS, tone, WN and post-cue periods in the high-threat context (n = 273 cells from 6 mice). **right**, Spearman correlation of speed and neuronal activity from the last 3 trials (preSCS, tone, WN and post-cue epochs, each point represents data from 1 s; n = 273 cells from 6 mice;  $r = 0.5187$ , 95% CI: 0.3696 to 0.6417,  $p < 0.0001$ ). **d**, Speed and neuronal activity aligned to the onset of flight bouts during WN in the high-threat context (n = 273 cells from 6 mice). **e**, Speed and neuronal activity aligned to the onset of freezing bouts during WN in the high-threat context (n = 273 cells from 6 mice). **f**, Spearman correlation plot for speed and Z-score from the identified freezing bouts (each dot represents values at each sec of the bouts,  $r = 0.657$ , 95% CI = -0.02019 to 0.1662,  $p = 0.175$ ). **g, left**, Z-scores of individual mice during preSCS, tone, WN and post-cue periods, across all trials (N = 6 mice; one-way ANOVA,  $F_{(3,20)} = 9.331$ ,  $P = 0.0005$ ; Bonferroni's multiple comparisons test). **right**, Z-scores of individual mice during first versus last 2 footshock periods (paired t-test,  $t = 0.2289$ ,  $df = 11$ , each dot represents an individual mouse during a single trial). **h**, The Z-scores of individual neurons during preSCS, tone, WN and post-cue periods, from the last trial in the high-threat context (n = 273 cells from 6 mice, one-way ANOVA,  $F_{(3,1112)} = 59.01$ ,  $P < 0.0001$ ; Bonferroni's multiple comparisons test). **i**, Freezing in the low-threat context (N = 6 mice; paired t-test,  $t = 3.424$ ,  $df=5$ ). **j**, Flight scores in the low-threat context. (N = 6

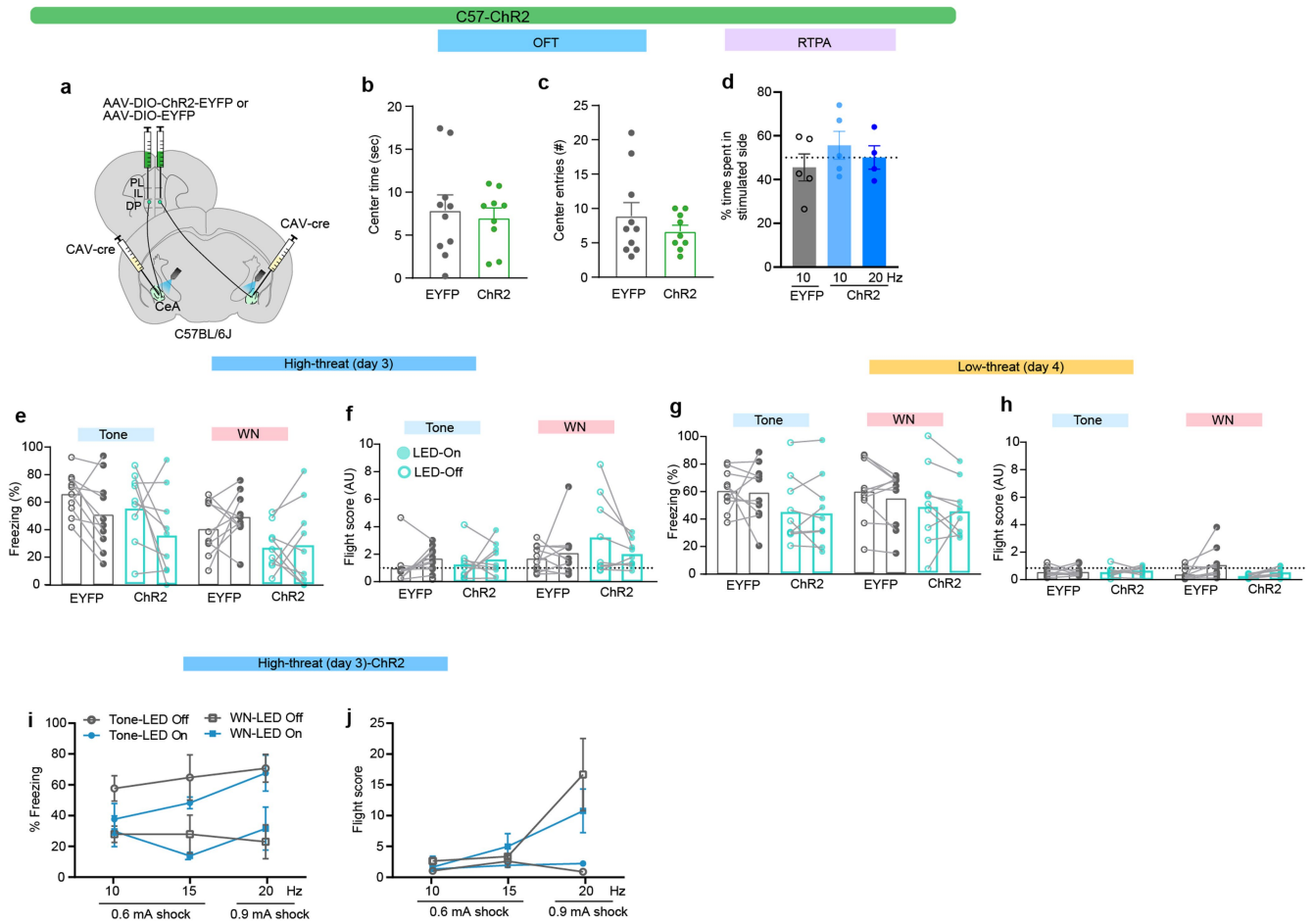
mice; paired t-test,  $t = 2.889$ ,  $df = 5$ ). **k, left**, Change in average speed and neuronal activity during preSCS, tone, WN and post-cue periods in the low-threat context over 4 trials (n = 273 cells from 6 mice). **right**, Spearman correlation of speed and neuronal activity from all recall trials in the low-threat context (preSCS, tone, WN and post cue epochs, each point represents 1 s of data; n = 273 cells from 6 mice;  $r = -0.07152$ , 95% CI: -0.2526 to 0.1144,  $p = 0.43$ ). **l**, Speed and neuronal activity aligned to the onset of flight bouts during WN in the low-threat context (n = 273 cells from 6 mice). **m**, Speed and neuronal activity aligned to the onset of freezing bouts during WN in the low-threat context (n = 273 cells from 6 mice). **n**, Spearman correlation of speed and neuronal activity from freezing bouts (n = 273 cells from 6 mice; each point represents one sec of data,  $r = 0.82$ , 95% CI = 0.02337 to 0.1669,  $P = 0.058$ ). **o**, Population activity from individual mice during preSCS, tone, WN and post-cue periods, across all trials (N = 6 mice; one-way ANOVA,  $F_{(3,20)} = 0.3923$ ,  $P = 0.75$ ). **p**, Neuronal activity of individual neurons during preSCS, tone, WN and post-cue periods, from the last trial in the low-threat context (n = 273 cells from 6 mice; one-way ANOVA,  $F_{(3,1008)} = 5.566$ ,  $P = 0.0009$ ; Bonferroni's multiple comparisons test). **q**, Z-scores of individual mice during context exposure (first 3 min baseline period) in high threat versus low-threat context (N = 6 mice; paired t-test,  $t = 2.705$ ,  $df=5$ ). Data in **a-c**, **d-e**, **h-k**, **l-m**, and **p** represented as means  $\pm$  s.e.m. Violin plots in **g** indicate median, interquartile range, and the distribution of individual data points. Two-sided statistical tests were used. \*\*\*\* $P < 0.0001$ , \*\*\* $P < 0.001$ , \*\* $P < 0.01$ , \* $P < 0.05$ .

# Article



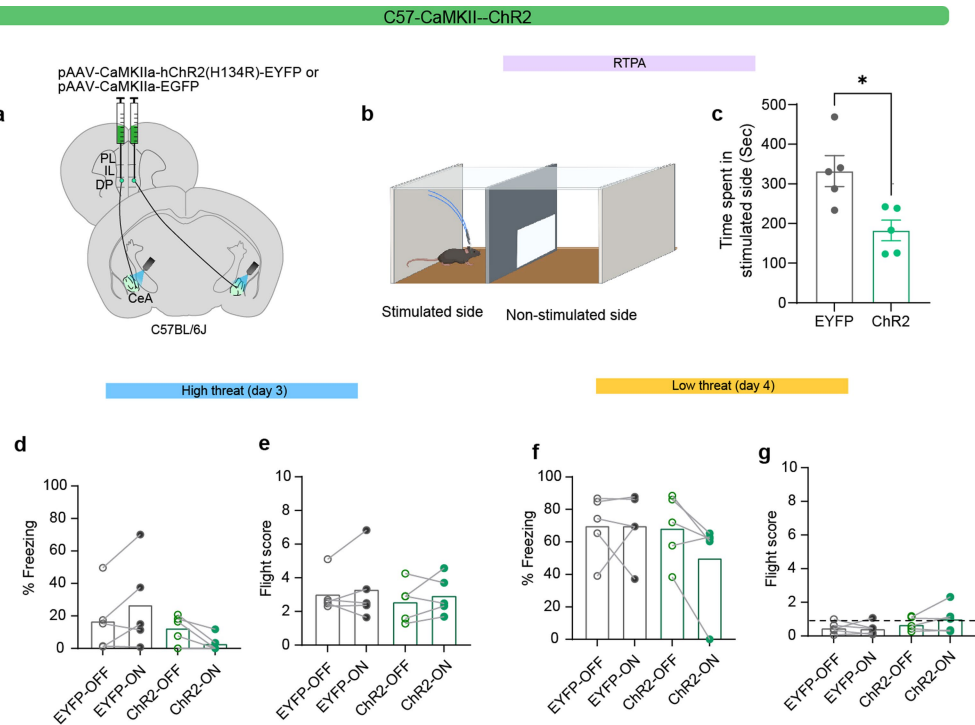
**Extended Data Fig. 4 | (Data related Fig. 4): Optogenetic inhibition of the DP-CEA pathway.** **a**, Intersectional approach used for optogenetic terminal inhibition of the DP-to-CeA neuronal projections. The image was adapted from the Allen Brain Atlas (Allen Institute for Brain Science). **b**, Experimental timeline. **c-e**, Effect of optogenetic inhibition on centre time (**c**), centre entries (**d**), and distance travelled (**e**) in the OFT (EYFP N = 9 mice, eNpHRN = 9 mice; unpaired t-test,  $t = 2.357$ ,  $df = 16$ ;  $t = 2.813$ ,  $df = 16$ ; and  $t = 0.7250$ ,  $df = 16$ , respectively). **f-h**, Effect of optogenetic inhibition on EYFP (N = 9) and eNpHR (N = 9) mice in the high-threat context on **f**, freezing (LED-on vs LED-off,

Mann-Whitney), **g**, flight (LED-on vs LED-off, Mann-Whitney), and **h**, speed during WN (Paired t-test  $t = 3.497$ ,  $df = 8$ ,  $p = 0.0081$ ). **i-k**, Effect of optogenetic inhibition in EYFP (N = 9) and eNpHR (N = 9) groups in the low-threat context on **i**, freezing (LED-on vs LED-off, Mann-Whitney, n.s.), **j**, flight (LED-on vs LED-off, Mann-Whitney) and **k**, speed during WN in the eNpHR group (Paired t-test,  $t = 2.619$ ,  $df = 8$ ,  $p = 0.307$ ). Data in **c-e** represented as mean  $\pm$  s.e.m. Data in **f-k** represented as mean with individual data points. Two-sided statistical tests were used. \*\* $P < 0.01$ , \* $P < 0.05$ .



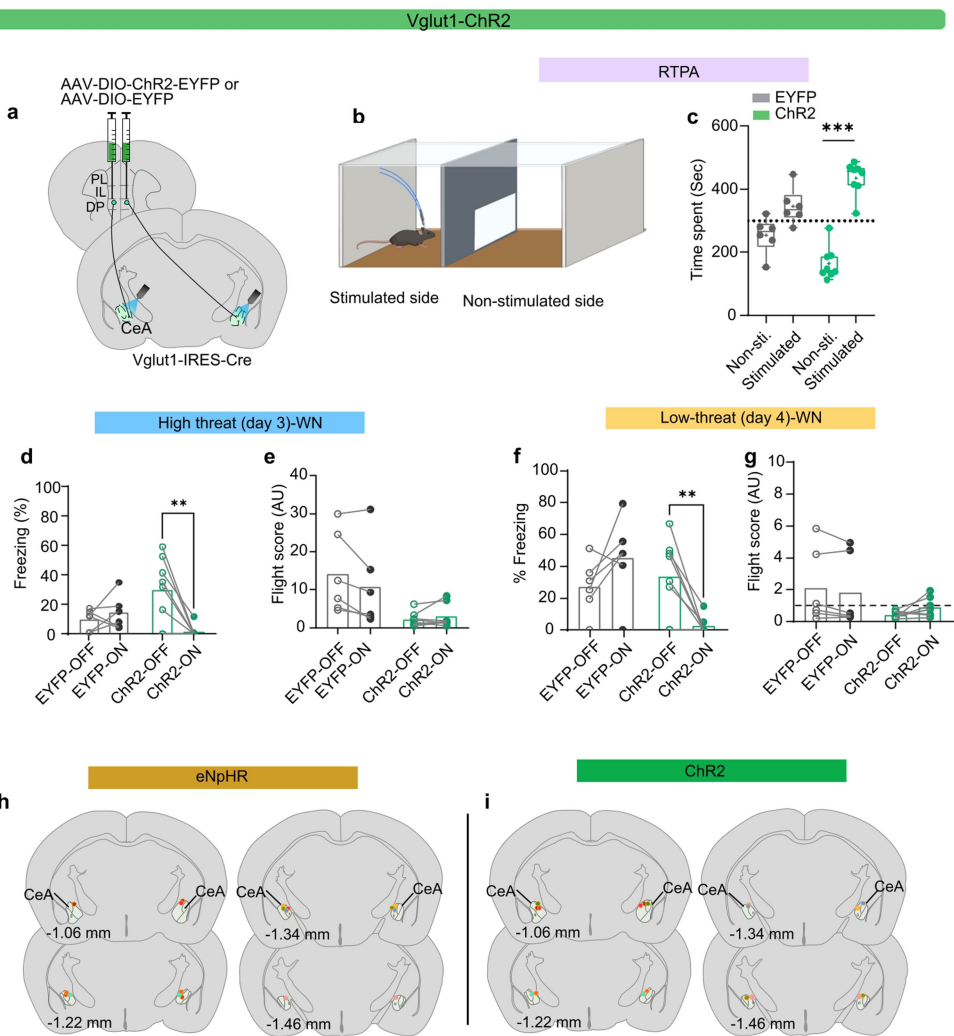
**Extended Data Fig. 5 | (Data related Fig. 4): Non-cell type specific stimulation of the DP-CEA pathway.** **a**, Intersectoral approach used to target optogenetic stimulation to DP-to-CeA terminals. The image was adapted from the Allen Brain Atlas (Allen Institute for Brain Science). **b-c**, Effect of optogenetic stimulation on OFT centre time (**b**) and centre entries (**c**) in EYFP (N = 10) and ChR2 (N = 9) groups (Unpaired t-test, n.s., t = 0.3950, df = 17, and t = 1.001, df = 17, respectively). **d**, Effects of optogenetic stimulation on real-time place avoidance in EYFP (10 Hz, N = 5) and ChR2 (10 Hz, N = 5; 20 Hz, N = 4) groups (One-way ANOVA  $F_{(2,11)} = 0.73, p = 0.502$ ). **e-f**, Effect of optogenetic excitation in EYFP (N = 10) and ChR2 (N = 9) groups in the high-threat context on **e**, freezing (LED-on vs LED-off, Mann-Whitney, n.s.) and **f**, flight (LED-on vs LED-off, Mann-Whitney, n.s.). **g-h**, Effect of optogenetic excitation in EYFP

(N = 10) and ChR2 (N = 9) groups in the low-threat context on **g**, freezing (LED-on vs LED-off, Mann-Whitney, n.s.) and **h**, flight (LED-on vs LED-off, Mann-Whitney, n.s.). **i-j**, Freezing (**i**) and flight scores (**j**) during optogenetic stimulation during day 3 at different stimulation frequencies and shock intensities (at 0.6 mA – 10 Hz, N = 9; 15 Hz, N = 3; at 0.9 mA – 20 Hz, N = 5; two-way ANOVA (for %freezing, Stimulation frequency x Shock intensity,  $F_{(6,56)} = 0.76, p = 0.601$ ; Stimulation frequency,  $F_{(2,56)} = 1.10, p = 0.339$ ; Shock intensity,  $F_{(3,56)} = 8.37, p = 0.0001$ ; for flight, Stimulation frequency x Shock intensity,  $F_{(6,56)} = 4.42, p = 0.001$ ; Shock intensity,  $F_{(3,56)} = 6.66, p = 0.001$ ; Bonferroni's post hoc test (tone/WN ON vs OFF non-significant). Data represented as mean ( $\pm$  s.e.m. in **b-d** and with individual data points in **i-j**). Two-sided statistical tests were used.

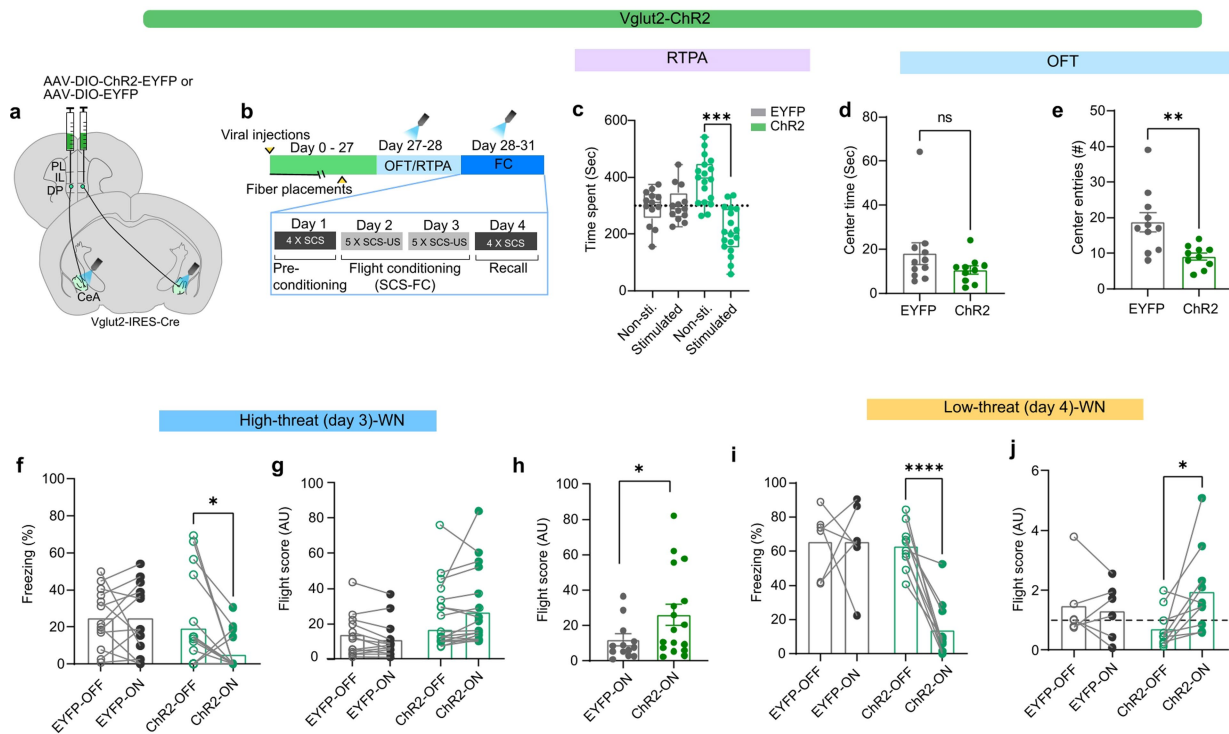


**Extended Data Fig. 6 | (Data related Fig. 4): Stimulation of the DP-CEA pathway using a CaMKII promotor.** **a**, Viral injection strategy for optogenetic terminal stimulation of DP-to-CeA neuronal projections. The image was adapted from the Allen Brain Atlas (Allen Institute for Brain Science). **b-c**, Schematic (**b**) and results (**c**) of real-time place aversion (RTPA) in EYFP (20 Hz, N = 5) and Chr2 (20 Hz, N = 5) groups (Unpaired t-test,  $t = 3.191$ ,  $df = 8$ ). The image in **b** was created with BioRender.com. **d-e**, Effect of optogenetic

excitation in EYFP (N = 5) and Chr2 (N = 5) groups in the high-threat context on **d**, freezing (LED-on vs LED-off, paired t-test, n.s.) and **e**, flight scores (LED-on vs LED-off, paired t-test, n.s.). **f-g**, Effect of optogenetic excitation in EYFP (N = 5) and Chr2 (N = 5) groups in the low-threat context on **f**, freezing (LED-on vs LED-off, paired t-test, n.s.) and **g**, flight scores (LED-on vs LED-off, paired t-test, n.s.). Data represented as mean  $\pm$  s.e.m. in **c** and with individual data points in **d-g**. Two-sided statistical tests were used. \*P < 0.05.

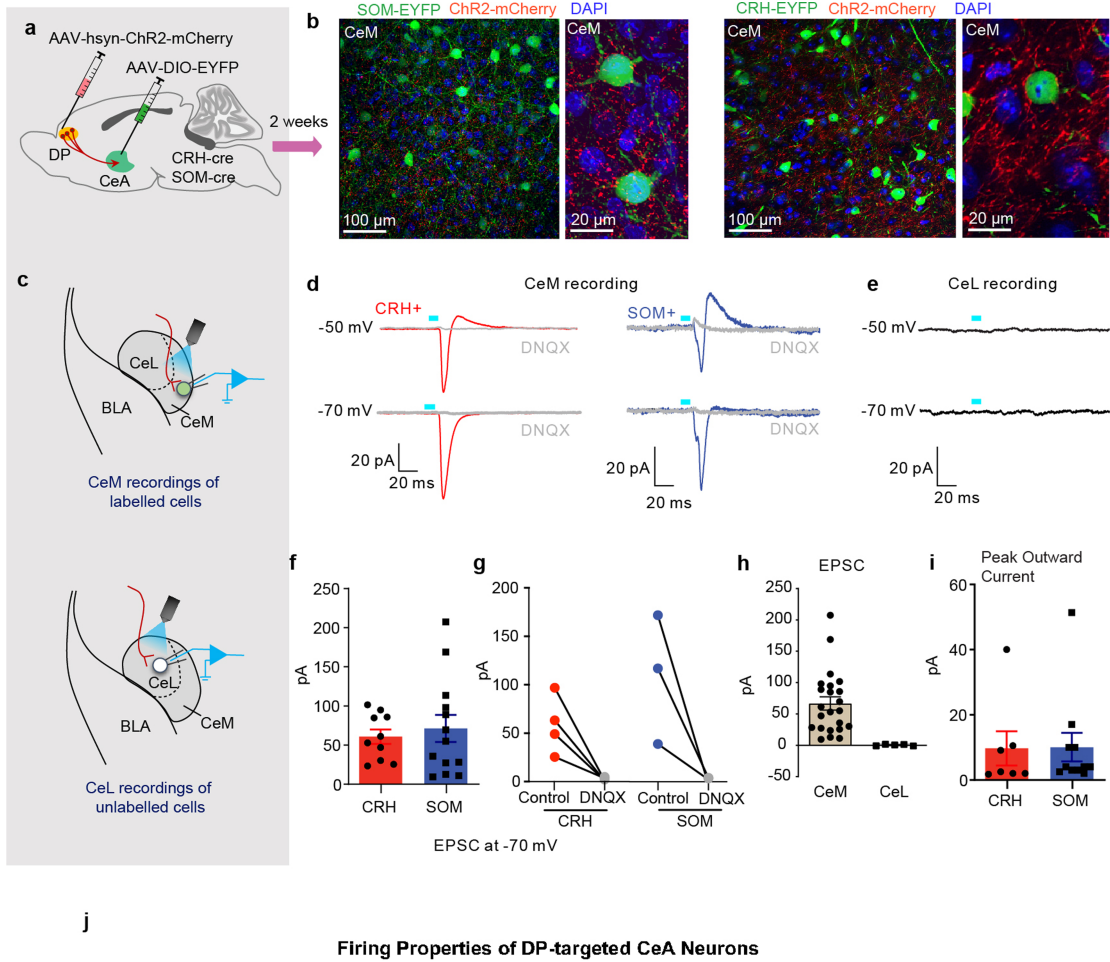


**Extended Data Fig. 7 | (Data related Fig. 4): Optogenetic stimulation of the Vglut1 + DP-CEA pathway.** **a**, Viral injection strategy for optogenetic terminal stimulation of DP-to-CeA neuronal projections. **b-c**, Schematic (**b**) and real-time place aversion (RTPA) performance (**c**) from EYFP (N = 6) and ChR2 (N = 8) groups (unpaired t-test, EYFP ( $t = 1.974$ ,  $df = 5$ ,  $P = 0.10$ ), ChR2 ( $t = 7.339$ ,  $df = 7$ )). The image in **b** was created with BioRender.com. **d-e**, Effect of optogenetic excitation in EYFP (N = 6) and ChR2 (N = 8) groups in the high-threat context on **d**, freezing during WN (LED-on vs LED-off, paired t-test, ChR2,  $t = 3.650$ ,  $df = 7$ ) and **e**, flight during WN (LED-on vs LED-off, paired t-test, ChR2,  $t = 1.077$ ,  $df = 7$ ,  $P = 0.31$ ). **f-g**, Effect of optogenetic excitation in EYFP (N = 6) and ChR2 (N = 8) groups in the low-threat context on **f**, freezing during WN (LED-on vs LED-off, paired t-test, ChR2,  $t = 3.748$ ,  $df = 7$ ) and **g**, flight score during WN (LED-on vs LED-off, paired t-test, ChR2,  $t = 2.211$ ,  $df = 7$ ,  $P = 0.06$ ). **h**, Example fibre placements over the CeA for the eNpHR groups (N = 9). **i**, Example fibre placements over the CeA for the ChR2 groups (N = 9). Box and whisker plots in **c** indicate median, interquartile range, and min. to max. of the distribution, crosses indicate means. Data in **d-g** represented as mean with individual data points. Two-sided statistical tests were used. \*\*\* $P < 0.001$ , \*\* $P < 0.01$ . The images in **a-h,i** were adapted from the Allen Brain Atlas (Allen Institute for Brain Science).



**Extended Data Fig. 8 | (Data related Fig. 4): Optogenetic stimulation of the Vglut2 + DP-CEA pathway.** **a**, Viral injection strategy for optogenetic terminal stimulation of DP-to-CeA neuronal projections. The image was adapted from the Allen Brain Atlas (Allen Institute for Brain Science). **b**, Experimental timeline. **c**, Real-time place aversion (RTPA) performance of EYFP ( $N=13$ ) and ChR2 ( $N=17$ ) groups (paired t-test, EYFP ( $t=0.2167$ ,  $df=12$ ,  $P=0.83$ ), ChR2 ( $t=4.713$ ,  $df=17$ )). **d-e**, Effect of optogenetic excitation on OFT centre time (**d**) and number of entries into the centre zone (**e**) in EYFP ( $N=11$ ) and ChR2 ( $N=10$ ) groups (unpaired t-test,  $t=3.288$ ,  $df=19$ ). **f-g**, Effect of optogenetic excitation in EYFP ( $N=13$ ) and ChR2 ( $N=17$ ) groups in the high-threat context on **f**, freezing during WN (LED-on vs LED-off, Wilcoxon

matched-pairs signed rank test, ChR2) and **g**, flight during WN (LED-on vs LED-off, Wilcoxon -test, ChR2,  $P=0.07$ ). **h**, Comparison of flight scores in the LED-on condition between EYFP control and ChR2 groups (Mann Whitney test,  $P=0.0349$ ). **i-j**, Effect of optogenetic excitation in EYFP ( $N=6$ ) and ChR2 ( $N=10$ ) groups in the low-threat context on **i**, freezing during WN (LED-on vs LED-off, paired t-test, ChR2,  $t=7.135$ ,  $df=9$ ) and **j**, flight scores during WN (LED-on vs LED-off, paired t-test, ChR2,  $t=t=2.717$ ,  $df=9$ ). Box and whisker plots in **c** indicate median, interquartile range, and min. to max. of the distribution, crosses indicate means. Data in **d-e** and **h** represented as mean  $\pm$  s.e.m, and as mean with individual data points in **f,g,i,j**. Two-sided statistical tests were used. \*\*\* $P < 0.001$ , \*\* $P < 0.01$ , \* $P < 0.05$ .

**j**

#### Firing Properties of DP-targeted CeA Neurons

DP-Excited cells (n=11)				
Classification	Spike Threshold (mV)	Spike Latency (ms)	Spike Frequency Adaptation (3rd ISI/Last ISI)	Sag (% steady-state)
Regular spiking (n=5)	-42 ± 2	46 ± 12	0.62 ± 0.11	17 ± 1
Bursting (n=4)	-43 ± 2	80 ± 40	—	21 ± 7
Late-firing (n=2)	-45 ± 6	194 ± 46	0.62 ± 0.04	11 ± 2

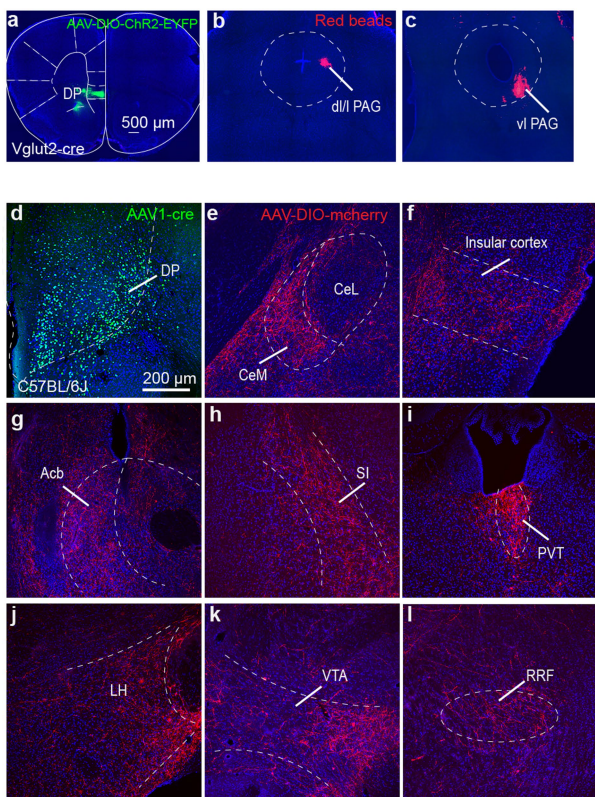
**Extended Data Fig. 9 | (Data related to Fig. 5): Optogenetically evoked responses in central amygdala neurons.** **a**, Schematic of targeting strategy.

**b**, DP terminals in CeM near SOM+ (*left*) and CRH+ (*right*) cells at 20x and 40x magnification. **c**, Strategy for recording light-evoked synaptic input from DP to SOM+ or CRH+ neurons from CeM (*top*) and CeL (*bottom*) regions.

**d**, Representative evoked synaptic responses in CeM SOM+ and CRH+ cells by photostimulation of DP axonal fibres in voltage-clamp. **e**, Photostimulation of axonal fibres did not evoke responses in CeL neurons. **f**, Average amplitude of evoked EPSCs in CRH+ neurons (N = 10 cells from 3 mice) and SOM+ (N = 13 cells from 3 mice) at -70 mV (unpaired Student's t-test,  $t = 0.4879$ ,  $df = 21$ ,  $p = 0.63$ ).

**g**, Amplitudes of evoked EPSCs in CRH+ (N = 4 cells from 3 mice) and SOM+ (N = 3 cells from 2 mice) neurons at -70 mV, before and after application of DNQX. **h**, Average amplitude of evoked EPSCs in CeM (N = 23 cells from 6 mice) and CeL neurons (N = 5 cells from 2 mice). **i**, The amplitude of disynaptic IPSCs evoked by ChR2 stimulation of DP terminals in CRH+ (N = 7 cells from 3 mice) and SOM+ (N = 11 cells from 2 mice; unpaired Student's t-test,  $t_{(16)} = 0.055$ ;  $p = 0.96$ ) neurons at -50 mV. **j**, The firing properties of DP-targeted CeM neurons. Data in **f**, **h**, **i** represented as mean ± s.e.m. Two-sided statistical tests were used. \*\*\*P < 0.001, \*\*P < 0.01, \*P < 0.05.

# Article



**Extended Data Fig. 10 | (Data related to Fig. 5): Brain regions targeted by CeM neurons receiving DP innervation.** **a**, Representative image showing ChR2 injection targeting in the DP. **b-c**, Representative images showing targeting of red beads to the **b**, dorsal (dl/l PAG) and **c**, ventrolateral (vlPAG) periaqueductal gray regions for electrophysiological recordings of PAG-projecting CeM neurons. **d**, Representative expression of EYFP in the DP of a C57BL/6J mouse injected with AAV1-cre-EYFP. **e**, Cre-dependent mCherry expression in the CeM of the same mouse. **f-l**, mCherry+ terminals of CeM neurons innervated by the DP project to insular cortex (**f**), nucleus accumbens (Acb, **g**), substantia innominata (SI, **h**), periventricular thalamus (PVT, **i**), lateral hypothalamus (LH, **j**), ventral tegmental area (VTA, **k**), and retrorubral field (RRF, **l**).

Corresponding author(s): Fadok, Jonathan

Last updated by author(s): Oct 25, 2023

## Reporting Summary

Nature Portfolio wishes to improve the reproducibility of the work that we publish. This form provides structure for consistency and transparency in reporting. For further information on Nature Portfolio policies, see our [Editorial Policies](#) and the [Editorial Policy Checklist](#).

### Statistics

For all statistical analyses, confirm that the following items are present in the figure legend, table legend, main text, or Methods section.

n/a Confirmed

- The exact sample size ( $n$ ) for each experimental group/condition, given as a discrete number and unit of measurement
- A statement on whether measurements were taken from distinct samples or whether the same sample was measured repeatedly
- The statistical test(s) used AND whether they are one- or two-sided  
*Only common tests should be described solely by name; describe more complex techniques in the Methods section.*
- A description of all covariates tested
- A description of any assumptions or corrections, such as tests of normality and adjustment for multiple comparisons
- A full description of the statistical parameters including central tendency (e.g. means) or other basic estimates (e.g. regression coefficient) AND variation (e.g. standard deviation) or associated estimates of uncertainty (e.g. confidence intervals)
- For null hypothesis testing, the test statistic (e.g.  $F$ ,  $t$ ,  $r$ ) with confidence intervals, effect sizes, degrees of freedom and  $P$  value noted  
*Give  $P$  values as exact values whenever suitable.*
- For Bayesian analysis, information on the choice of priors and Markov chain Monte Carlo settings
- For hierarchical and complex designs, identification of the appropriate level for tests and full reporting of outcomes
- Estimates of effect sizes (e.g. Cohen's  $d$ , Pearson's  $r$ ), indicating how they were calculated

*Our web collection on [statistics for biologists](#) contains articles on many of the points above.*

### Software and code

Policy information about [availability of computer code](#)

Data collection Plexon- Studio V3(recording), Editor V3 (video analysis), Radiant V2 (optogenetics), Medassociates (V5), Neuroexplorer (V5) , Olympus Confocal (FV31S-SW version 2.4.1.198), Zeiss axio scan.z1 (ZEN2), Miniscope controller (Miniscope DAQ software V3.2)

Data analysis Graphpad Prism 10 (Statistics), R 4.1.0 (graph), CIAtah (calcium Imaging), Matlab R2018b (Calcium Imaging), ImageJ (1.52a)

For manuscripts utilizing custom algorithms or software that are central to the research but not yet described in published literature, software must be made available to editors and reviewers. We strongly encourage code deposition in a community repository (e.g. GitHub). See the Nature Portfolio [guidelines for submitting code & software](#) for further information.

### Data

Policy information about [availability of data](#)

All manuscripts must include a [data availability statement](#). This statement should provide the following information, where applicable:

- Accession codes, unique identifiers, or web links for publicly available datasets
- A description of any restrictions on data availability
- For clinical datasets or third party data, please ensure that the statement adheres to our [policy](#)

All data supporting the findings of this study are available within the paper and its Supplementary Information

## Research involving human participants, their data, or biological material

Policy information about studies with [human participants or human data](#). See also policy information about [sex, gender \(identity/presentation\), and sexual orientation](#) and [race, ethnicity and racism](#).

Reporting on sex and gender

N/A

Reporting on race, ethnicity, or other socially relevant groupings

N/A

Population characteristics

N/A

Recruitment

N/A

Ethics oversight

N/A

Note that full information on the approval of the study protocol must also be provided in the manuscript.

## Field-specific reporting

Please select the one below that is the best fit for your research. If you are not sure, read the appropriate sections before making your selection.

Life sciences       Behavioural & social sciences       Ecological, evolutionary & environmental sciences

For a reference copy of the document with all sections, see [nature.com/documents/nr-reporting-summary-flat.pdf](https://nature.com/documents/nr-reporting-summary-flat.pdf)

## Life sciences study design

All studies must disclose on these points even when the disclosure is negative.

Sample size

Sample size was determined based on the previous literature using similar experimental approach (Fadok et al 2017, Tovote et al 2016; Parker et al 2018)

Data exclusions

All exclusion criteria were established prior to data collection: Mice showing poor viral expression or missed targeting for implantation of the lens or fiber were excluded prior to conducting analyses.

Replication

The exact number of repetitions (individual data points from separate cells and/or animals) are indicated in figures or figure legends. All attempts at replication were successful in 9–10 animals. Main effects were consistent across mice. All protocols used for the experiments are described in detail in the Methods section and supplementary material, and further information can be requested from the corresponding authors to ensure replication in other laboratories.

Randomization

Blocked randomization was used to allocate animals to the different experimental groups.

Blinding

Blinded observers to the experimental condition were used for behavioral and histological data analysis

## Reporting for specific materials, systems and methods

We require information from authors about some types of materials, experimental systems and methods used in many studies. Here, indicate whether each material, system or method listed is relevant to your study. If you are not sure if a list item applies to your research, read the appropriate section before selecting a response.

### Materials & experimental systems

n/a	Involved in the study
<input type="checkbox"/>	<input checked="" type="checkbox"/> Antibodies
<input checked="" type="checkbox"/>	<input type="checkbox"/> Eukaryotic cell lines
<input checked="" type="checkbox"/>	<input type="checkbox"/> Palaeontology and archaeology
<input type="checkbox"/>	<input checked="" type="checkbox"/> Animals and other organisms
<input checked="" type="checkbox"/>	<input type="checkbox"/> Clinical data
<input checked="" type="checkbox"/>	<input type="checkbox"/> Dual use research of concern
<input checked="" type="checkbox"/>	<input type="checkbox"/> Plants

### Methods

n/a	Involved in the study
<input checked="" type="checkbox"/>	<input type="checkbox"/> ChIP-seq
<input checked="" type="checkbox"/>	<input type="checkbox"/> Flow cytometry
<input checked="" type="checkbox"/>	<input type="checkbox"/> MRI-based neuroimaging

## Antibodies

### Antibodies used

The primary antibodies used were- rabbit anti-RFP (Cat# 600-401-379, Rockland Immunochemicals, USA; Zhang C et al. (2022; PMID: 35705049)), chicken anti-GFP (Cat# NB100-1614, Novus Biologicals, USA; Lloyd-Lewis et al (2022; PMID: 35263603)), rabbit anti-cFos (Cat# 226003, Synaptic Systems, Germany, Bijoch et al (2023; PMID: 36683039)). The secondary antibodies used were donkey anti-rabbit AlexaFluor 555 (Cat #A31572; Roggeri et al (2023; PMID: 37830557)) and goat anti-rabbit AlexaFluor 488 (Cat # A11034; Mass et al (2023; PMID: 37817932)) or goat anti-chicken AlexaFluor 488 (Cat # A-11039; Tan et al (2023; PMID: 37707499)), Thermo Fisher Scientific, USA) from Thermo Fisher Scientific, USA.

### Validation

These antibodies have been validated by the manufacturer and in the previous literature.  
 1) Rabbit anti-RFP (Cat# 600-401-379, Zhang C et al. (2022; PMID: 35705049)): Polyclonal anti-RFP is designed to detect RFP and its variants. This antibody has been tested by ELISA, Western blot, IF, and IHC, and is suitable for use in EM, FC, FISH, IP, and multiplex assays based on published references. Assay by immunoelectrophoresis resulted in a single precipitin arc against anti-Rabbit Serum and purified and partially purified Red Fluorescent Protein (Discosoma)  
 2) Chicken anti-GFP (Cat# NB100-1614, Lloyd-Lewis et al (2022; PMID: 35263603)): Publications tested in 9 confirmed species: Human, Mouse, Rat, Drosophila, Firefly, Jellyfish, Primate, Yeast, Zebrafish and tested in 9 applications: ICC/IF, IF/IHC, IHC, IHC-Fr, IHC-FrFl, IHC-P, IHC/IF, In Vivo, WB. NB100-1614 has been tested on transgenic mice expressing recombinant GFP  
 3) Rabbit anti-cFos (Cat# 226003, Synaptic Systems, Germany, Bijoch et al (2023; PMID: 36683039)): This antibody was tested in previous literature in rodents including mice for IHC applications.

## Animals and other research organisms

Policy information about [studies involving animals](#); [ARRIVE guidelines](#) recommended for reporting animal research, and [Sex and Gender in Research](#)

### Laboratory animals

Male and female (8-12 weeks old) C57BL/6J (Stock No: 000664, Jackson laboratories, USA) mice were used. We also used CRH-IRES-Cre (Stock Number: 012704), SOM-IRES-Cre (Stock No: 013044), Vglut1-IRES-Cre (Stock No: 023527), and Vglut2-ires-cre (Stock Number: 028863) mice.

### Wild animals

No wild animals were used in the study

### Reporting on sex

All data are derived from both males and females.

### Field-collected samples

Did not involve samples collected from the field.

### Ethics oversight

This study is conducted under the observation of Tulane Institutional Animal Care and Use Committee (IACUC).

Note that full information on the approval of the study protocol must also be provided in the manuscript.